Monthly Notices of the ROYAL ASTRONOMICAL SOCIETY

MNRAS **504,** 5788–5805 (2021) doi:10.1093/mnras/stab1167
Advance Access publication 2021 April 26

Characterization of 92 southern *TESS* candidate planet hosts and a new photometric [Fe/H] relation for cool dwarfs

Adam D. Rains [1★] Maruša Žerjal [1] Michael J. Ireland [1] Thomas Nordlander [1,2] Michael S. Bessell [1] Luca Casagrande [1,2] Christopher A. Onken [1,3] Meridith Joyce [1,2] Jens Kammerer[1,4] and Harrison Abbot[1]

[1]*Research School of Astronomy and Astrophysics, Australian National University, Canberra, ACT 2611, Australia*
[2]*ARC Centre of Excellence for All Sky Astrophysics in 3 Dimensions (ASTRO 3D)*
[3]*Centre for Gravitational Astrophysics, Research Schools of Physics, and Astronomy and Astrophysics, Australian National University, Canberra, ACT 2611, Australia*
[4]*European Southern Observatory, Karl-Schwarzschild-Str 2, D-85748 Garching, Germany*

Accepted 2021 April 16. Received 2021 April 16; in original form 2021 February 14

ABSTRACT

We present the results of a medium-resolution optical spectroscopic survey of 92 cool ($3000\,\mathrm{K} \lesssim T_{\rm eff} \lesssim 4500\,\mathrm{K}$) southern *TESS* candidate planet hosts, and describe our spectral fitting methodology used to recover stellar parameters. We quantify model deficiencies at predicting optical fluxes, and while our technique works well for $T_{\rm eff}$, further improvements are needed for [Fe/H]. To this end, we developed an updated photometric [Fe/H] calibration for isolated main-sequence stars built upon a calibration sample of 69 cool dwarfs in binary systems, precise to ±0.19 dex, from supersolar to metal poor, over $1.51 < Gaia\,(B_P - R_P) < 3.3$. Our fitted $T_{\rm eff}$ and $R_\star$ have median precisions of 0.8 per cent and 1.7 per cent, respectively, and are consistent with our sample of standard stars. We use these to model the transit light curves and determine exoplanet radii for 100 candidate planets to 3.5 per cent precision and see evidence that the planet radius gap is also present for cool dwarfs. Our results are consistent with the sample of confirmed *TESS* planets, with this survey representing one of the largest uniform analyses of cool *TESS* candidate planet hosts to date.

Key words: techniques: spectroscopic – planets and satellites: fundamental parameters – stars: fundamental parameters – stars: low-mass.

1 INTRODUCTION

Low-mass stars are the most common kind of star in the Galaxy, comprising more than two-thirds of all stars (Chabrier 2003), and dominating the Solar Neighbourhood population (e.g. Henry, Kirkpatrick & Simons 1994; Henry et al. 2006, 2018; Winters et al. 2015). This abundance alone makes them prime targets for planet searches, with microlensing surveys, which have very little bias on host star masses, revealing that there is at least one bound planet per Milky Way star (Cassan et al. 2012). Results from the *Kepler* mission (Borucki et al. 2010) also bear this out, showing that a large number of planets remain undiscovered around cool dwarfs (Morton & Swift 2014), and that such cool stars are actually more likely to host small planets ($2 < R_{\rm P} < 4\,\mathrm{R}_\oplus$, where $R_{\rm P}$ and $\mathrm{R}_\oplus$ are the planet and earth radii, respectively) than their hotter counterparts (Howard et al. 2012; Dressing & Charbonneau 2015).

However, the inherent faintness of these stars complicates the study of both them and their planets. While we now know of over 4000 confirmed planets orbiting stars other than our own (overwhelmingly discovered by transiting exoplanet surveys), almost an equal number await confirmation.[1] Exoplanet transit surveys like *Kepler* and *TESS* (Ricker et al. 2015) are able to place tight constraints on planetary radii given a known stellar radius, but follow-up precision radial velocity observations are required to provide planetary mass constraints. This is the second reason why planet searches around low-mass stars are critical: Their smaller radii and lower masses make the transit signals and radial velocities of higher amplitudes for any planets they host as compared to the same planets around more massive host stars. This is especially important when looking for planets with terrestrial radii or masses, respectively.

Many planet host stars have never been targeted by a spectroscopic survey, leaving their properties to be estimated through photometry alone. For instance, the *TESS* input catalogue (Stassun et al. 2018, 2019) based its stellar parameters primarily on photometry, having spectroscopic properties for only about 4 million stars of the nearly 700 million with photometrically estimated equivalents. While stars warmer than 4000 K are well suited to bulk estimation of properties from photometry (see e.g. Carrillo et al. 2020), special care must be taken for cool dwarfs whose faintness and complex atmospheres make such relations more complex to develop and implement (e.g. see Muirhead et al. 2018, for the K and M dwarf specific approach taken from the *TESS* input catalogue).

NASA's *TESS* mission, by virtue of being all-sky, has given us a wealth of bright candidates that are now being actively followed up by ground-based spectroscopic surveys. While multi-epoch radial velocity observations are required to determine planetary masses, these surveys are typically biased towards the brightest stars and smallest planets. As such, there remains a need for single-epoch spectroscopic follow-up of fainter targets to provide reliable host star

★ E-mail: adam.rains@anu.edu.au
[1]https://exoplanetarchive.ipac.caltech.edu/

properties (primarily $T_{\rm eff}$, log g, [Fe/H], and the stellar radius $R_\star$) and allow radial constraints to be placed on transiting planet candidates. Indeed, the LAMOST Survey (Zhao et al. 2012) undertook targeted low resolution spectroscopic follow-up of stars in the *Kepler* field (De Cat et al. 2015) with the goal of deriving spectroscopic stellar properties. Considering the goal of planet radii determination specifically, Dressing et al. (2019) used medium-resolution near-infrared (NIR) spectra, and Wittenmyer et al. (2020) high-resolution optical spectra to follow up *K2* (Howell et al. 2014) transiting planet candidate hosts and place radius constraints on both planets and their hosts.

Even without mass estimates, much can be learned about exoplanet demographics from their radii alone. As demonstrated by Fulton et al. (2017), Fulton & Petigura (2018), Van Eylen et al. (2018), Kruse et al. (2019), Hardegree-Ullman et al. (2020), Cloutier & Menou (2020), and Hansen et al. (2021), having a large sample of precise planet radii allows insight into the exoplanet radius distribution, which appears to be bimodal with an observable gap in the super-Earth regime ($\sim$1.8 $R_\oplus$). This is thought to be the result of physical phenomena like photoevaporation (where flux from the parent star strips away weakly held atmospheres, e.g. Owen & Wu 2013, 2017; Lee, Chiang & Ormel 2014; Lopez & Fortney 2014; Lee & Chiang 2016; Lopez & Rice 2018) or core-powered mass-loss (where a cooling rocky core erodes light planetary atmospheres via its cooling luminosity, e.g. Ikoma & Hori 2012; Ginzburg, Schlichting & Sari 2018; Gupta & Schlichting 2019, 2020), and its location likely has a dependence on stellar host mass (e.g. Cloutier & Menou 2020). As such, improving the sample of planets with radius measurements allows us to place observational constraints on planet formation channels and the mechanisms that sculpt planets throughout their lives.

The scientific importance of searching for planets around low-mass stars to study their demographics is thus clear. However, the exact approach for understanding the stars themselves is less obvious, as cool dwarfs are not as well understood as their prevalence would suggest. Their inherent faintness and atmospheric complexity have led to long-standing issues observing representative sets of standard stars, generating synthetic spectra accounting for molecular absorption as well as consistently modelling their evolution (see e.g. Allard et al. 1997; Chabrier 2003).

Analysis of spectra from warmer stars is made simpler by the existence of regions of spectral continuum where atomic or molecular line absorption is minimal, allowing one to disentangle within reasonable uncertainties the effect of [Fe/H] and $T_{\rm eff}$ on an emerging spectrum. This is not the case for cool dwarfs for which there is no continuum at shorter wavelengths, with the deepest absorption caused by most notably TiO in the optical and water in the NIR, but also various other oxides or hydrides. The strength of these features is a function of *both* temperature and [Fe/H], making it difficult to ascribe a unique $T_{\rm eff}$–[Fe/H] pair to a given star.

Despite this complexity, it is possible to take advantage of the relative [Fe/H] insensitivity of NIR K-band magnitudes alongside [Fe/H]-sensitive optical photometry to probe cool dwarf [Fe/H]. This was predicted by theory (see e.g. Allard et al. 1997; Baraffe et al. 1998; Chabrier & Baraffe 2000, for summaries), confirmed observationally (Delfosse et al. 2000), and later formalized into various empirical calibrations (Bonfils et al. 2005; Johnson & Apps 2009; Schlaufman & Laughlin 2010; Neves et al. 2012; Hejazi, De Robertis & Dawson 2015; Dittmann et al. 2016).

The last decade has seen a number of studies using low–medium-resolution (mostly NIR) spectra, often focused on the development of [Fe/H] relations based on spectral indices (e.g. optical–NIR: Mann et al. 2013b, 2015; Mann, Gaidos & Ansdell 2013c; Kuznetsov et al. 2019; NIR: Newton et al. 2014; H band: Terrien et al. 2012; K band: Rojas-Ayala et al. 2010, 2012). Other studies have opted to use high-resolution spectra, which gives access to unblended atomic lines that are not accessible to lower resolution observations (e.g. optical: Bean et al. 2006a; Bean, Benedict & Endl 2006b; Rajpurohit et al. 2014; Passegger, Wende-von Berg & Reiners 2016; Y band: Veyette et al. 2017; optical–NIR: Woolf & Wallerstein 2005, 2006; Passegger et al. 2018; J band: Önehag et al. 2012; H band: Souto et al. 2017).

Finally, on the point of M-dwarf evolutionary models (and low-mass, cool main-sequence stars more generally), there has long been contention between model radii and observed radii (e.g. Kraus et al. 2015). This is often attributed to magnetic fields (and/or the mixing length parameter, which simplistically parametrizes the effects of magnetic fields among other energy transport mechanisms in 1D stellar structure and evolution programs) and is related to the difficulty in accurately modelling convection (e.g. Feiden & Chaboyer 2012; Joyce & Chaboyer 2018). Fortunately, due to the aforementioned insensitivity of NIR K-band photometry to [Fe/H], empirical mass and radius relations have been developed and calibrated on interferometric diameters and dynamical masses (e.g. Henry & McCarthy 1993; Delfosse et al. 2000; Mann et al. 2015, 2019; Benedict et al. 2016).

Here, we conduct a moderate-resolution spectroscopic survey of 92 southern cool ($T_{\rm eff} \lesssim 4500$ K) *TESS* candidate planet hosts with the wide-field spectrograph (WiFeS) instrument (Dopita et al. 2007) on the ANU 2.3 m Telescope at Siding Spring Observatory (NSW, Australia). We combine our spectroscopic observations with literature optical photometry and trigonometric parallaxes from *Gaia* data release (DR) 2 (Gaia Collaboration 2016; Brown et al. 2018), infrared photometry from 2MASS (Skrutskie et al. 2006), optical photometry from SkyMapper DR3 (Keller et al. 2007; Onken et al. 2019; DR3 DOI: 10.25914/5f14eded2d116), empirical relations from Mann et al. (2015, 2019), and synthetic MARCS model atmospheres (Gustafsson et al. 2008) in order to produce stellar $T_{\rm eff}$, log g, [Fe/H], bolometric flux ($f_{\rm bol}$), $R_\star$, and stellar mass ($M_\star$). By modelling the transit light curves of these host stars, we are additionally able to produce precision planetary radii for 100 candidate planets, which represents one of the largest uniform analyses of cool *TESS* hosts to date. Our observations and data reduction are described in Section 2, our photometric [Fe/H] relation in Section 3, our host star characterization methodology and resulting parameters in Section 4, our transit light-curve fitting and results in Section 5, discussion of results in Section 6, and concluding remarks in Section 7.

2 OBSERVATIONS AND DATA REDUCTION

2.1 Target selection

Our initial target selection of southern cool dwarf TOIs was done in 2019 August, including stars with $T_{\rm eff} \leq 4500$ K in the *TESS* input catalogue and unblended 2MASS photometry. In order to have reliable parallaxes, we impose the additional requirement that our stars have a *Gaia* DR2 Renormalized Unit Weight Error (RUWE)[2] of $<$1.4, as recommended by the *Gaia* team.[3] Adding extra targets sourced in 2020 August, and removing those identified

[2]Expected to be approximately 1.0 in case where the single star model provides a good fit for the astrometric data. See https://gea.esac.esa.int/archive/documentation/GDR2/Gaia_archive/chap_datamodel/sec_dm_main_tables/ssec_dm_ruwe.html.

[3]Though we do accept TIC 158588995 with a marginal RUWE$\sim$1.47 as it sits on the main sequence and does not appear overluminous.

as false positives through community follow-up observations (as listed on NASA's Exoplanet Follow-up Observing Program for *TESS*, ExoFOP-*TESS*, website[4]), we are left with a sample of 92 southern candidate planet hosts spread across the sky with $8.7 <$ apparent *Gaia* $G < 15.8$. These targets are listed in Table 1, and plotted on a colour–magnitude diagram in Fig. 1, noting that a few appear distinctly above the main sequence. These stars are thus overluminous because they are young and still contracting to the main sequence or because they are unresolved binaries.

All our targets have *Gaia* DR2 G, B_P, R_P, and 2MASS J, H, K_S photometry, and most have at least one of SkyMapper DR3 r, i, z (noting that the survey is still ongoing, so not all bands are available for all targets). We calculate distances from *Gaia* DR2 parallaxes, incorporating the systematic parallax offset of $-82 \pm 33\,\mu$as found by Stassun & Torres (2018).

To correct for reddening, we use the 3D dust map of Leike, Glatzle & Enßlin (2020), implemented within the python package `dustmaps` (Green 2018). Targeting bright, cool dwarfs as we do here automatically means that our stars will be relatively close, and we take those within the Local Bubble, two-thirds of our sample, to be unreddened ($\lesssim$70 pc; e.g. Leroy 1993; Lallement et al. 2003) so long as the *Gaia* G-band extinction reported by the dust map is consistent with zero ($A_G < 0.01$). Nominal extinction coefficients were sourced from Casagrande & VandenBerg (2014) for the 2MASS JHK_S bands and Casagrande et al. (2019) for SkyMapper *uvgriz*, with *Gaia* G, B_P, and R_P coefficients computed from the relation given in Casagrande et al. (2020) for $B_P - R_P = 2.03$, the median value for our sample.

2.2 Standard selection

Given the complexities involved in determining the properties of cool dwarfs, we also observed a set of 136 well-characterized late K/M-dwarf standards from the literature. Broadly, these standards have parameters from at least one of the following sources:

(i) [Fe/H] from a companion with spectral type FGK,
(ii) [Fe/H] from low-resolution NIR spectra,
(iii) $T_{\rm eff}$ from interferometry.

With the exception of available interferometric $T_{\rm eff}$ standards, we additionally wanted to source standards from large uniform catalogues due to the known problem of systematics between different spectroscopic techniques (e.g. Lebzelter et al. 2012; Hinkel et al. 2016). With this in mind, the bulk of our M/late-K dwarf standards come from the works of Rojas-Ayala et al. (2012) and Mann et al. (2015), with interferometric targets from von Braun et al. (2012, 2014), Boyajian et al. (2012), Rabus et al. (2019), and Rains et al. (2020) and FGK companion [Fe/H] compiled by Newton et al. (2014) from Valenti & Fischer (2005), Sousa et al. (2006), and Sozzetti et al. (2009). Our mid-K dwarf calibrators do not come from a single uniform catalogue; they are instead pulled from the works of Woolf & Wallerstein (2005), Sousa et al. (2008, 2011), Prugniel, Vauglin & Koleva (2011), Tsantaki et al. (2013), Luck (2017, 2018), and Montes et al. (2018).

These stars were observed with the same instrument settings as our science targets [but at higher signal-to-noise ratio (SNR)], with the intent to provide checks against our analysis techniques for this notoriously complex set of stars.

[4]https://exofop.ipac.caltech.edu/tess/

2.3 Spectroscopic observations

Observations were conducted using the WiFeS instrument (Dopita et al. 2007) on the ANU 2.3 m Telescope at Siding Spring Observatory, Australia between 2019 August and 2020 September. WiFeS, a dual-camera integral field spectrograph, is an effective stellar survey instrument due to its high throughput and broad wavelength coverage. Using the B3000 and R7000 gratings, and RT480 beam splitter, we obtain low-resolution blue spectra ($3500 \leq \lambda \leq 5700$ Å, $\lambda/\Delta\lambda \sim 3000$) and moderate-resolution red spectra ($5400 \leq \lambda \leq 7000$ Å, $\lambda/\Delta\lambda \sim 7000$) with median signal-to-noise ratios (SNRs) per spectral pixel of 16 and 58, respectively. Exposure times ranged from 20 s to 30 min, and were chosen on the basis of 0.5 mag bins in *Gaia* G.

Target observations were bracketed hourly with NeAr Arc lamp exposures, telluric standards were observed every few hours, and flux standards were observed several times throughout each night. Data reduction was done using the standard PyWiFeS pipeline (Childress et al. 2014) with the exception of custom flux calibration due to PyWiFeS' poor performance with R7000 spectra. Science target observations are listed in Table A1, and standard star observations in Table B1.

2.4 Radial velocity determination

Radial velocities of the WiFeS R7000 spectra were determined from a least-squares minimization of a set of synthetic template spectra varying in temperature (see Section 4.1 for details of model grid). We use a coarsely sampled version of this grid, computed at $R \sim 7000$ over $5400 \leq \lambda \leq 7000$ for $3000 \leq T_{\rm eff} \leq 5500$ K, $\log g = 4.5$, and [Fe/H]=0.0, with $T_{\rm eff}$ steps of 100 K for radial velocity determination. For further information on our RV fitting formalism, see Žerjal et al. (2021).[5]

Statistical uncertainties on this approach are median $\sim 410\,{\rm m\,s^{-1}}$, though comparison to *Gaia* DR2 in Fig. 2 reveals a larger scatter with a standard deviation of $\sim$4.5 km s^{-1}, computed from a median absolute deviation, which we add in quadrature with our statistical uncertainties. Higher uncertainties are consistent with the work of Kuruwita et al. (2018), who found that WiFeS varies on shorter time-scales than our hourly arcs can account for. While they additionally improved precision by calibrating using oxygen B-band absorption, RV uncertainties of $\sim$4.5 km s^{-1} are sufficient for this work. Our final values are reported in Table A1 for science targets, and Table B1 for standards.

3 PHOTOMETRIC METALLICITY CALIBRATION

As established earlier, cool dwarf metallicities are notoriously difficult to determine, particularly when working with optical spectra. Bonfils et al. (2005) initially proposed empirical calibrations to determine [Fe/H] from a star's position in $M_K - (V - K)$ space, a technique that was later iterated on by Johnson & Apps (2009), Schlaufman & Laughlin (2010), and Neves et al. (2012). Such relations are based on the fact that once on the main sequence, low-mass stars do not evolve (and hence change in brightness and temperature) appreciably on moderate time-scales as compared to their higher mass and faster evolving counterparts. Thus, assuming no extra scatter from unresolved binaries and standard helium enrichment (e.g. Pagel & Portinari 1998), a star's position above

[5]Our RV fitting code, along with all other codes for this project, can be found at https://github.com/adrains/plumage.

Table 1. Science targets.

TOI[a]	TIC[b]	2MASS[c]	*Gaia* DR2[d]	RA[d] (hh mm ss.ss)	Dec.[d] (dd mm ss.ss)	G^d (mag)	$B_p - R_p{}^d$ (mag)	Plx[d] (mas)	RUWE[d]	$E(B-V)$	$N^e_{\rm pc}$
741	359271092	09213761-6016551	5299440441521812992	09 21 35.86	−61 43 07.68	8.68	2.03	95.63 ± 0.03	1.1	0.00	1
731	34068865	09442986-4546351	5412250540681250560	09 44 29.16	−46 13 15.60	9.15	2.32	106.21 ± 0.03	1.1	0.00	1
260	37749396	00190556-0957530	2428162410789155328	00 19 05.52	−10 02 01.68	9.31	1.70	49.51 ± 0.06	0.9	0.00	1
836	440887364	15001942-2427147	6230733559097425152	15 00 19.18	−25 32 44.88	9.39	1.55	36.33 ± 0.04	1.0	0.01	2
562	413248763	09360161-2139371	5664814198431308288	09 36 01.80	−22 20 05.64	9.88	2.40	105.88 ± 0.06	1.1	0.00	3
455	98796344	03015142-1635356	5153091836072107136	03 01 51.00	−17 24 19.80	10.05	2.59	145.55 ± 0.08	1.1	0.00	2
139	62483237	22253655-3454346	6598814657249555328	22 25 36.58	−35 05 25.08	10.08	1.45	23.55 ± 0.04	1.0	0.00	1
253	322063810	00571629-5135048	4928367189956040960	00 57 16.44	−52 24 52.92	10.18	1.71	32.39 ± 0.03	1.0	0.00	1
134	234994474	23200751-6003545	6491962296196145664	23 20 06.86	−61 56 03.48	10.23	2.03	39.73 ± 0.04	1.0	0.00	1
544	50618703	05290957-0020331	3220926542276901888	05 29 09.62	−1 39 25.56	10.40	1.57	24.29 ± 0.04	1.1	0.01	1
486	260708537	06334998-5831426	5482827676662168832	06 33 49.18	−59 28 30.00	10.53	2.43	65.70 ± 0.03	1.2	0.00	1
177	262530407	01214538-4642518	4933912198893332224	01 21 45.22	−47 17 07.08	10.55	2.17	44.46 ± 0.05	1.0	0.00	1
129	201248411	00004490-5449498	4923860051276772608	00 00 44.54	−55 10 09.12	10.59	1.39	16.16 ± 0.02	1.1	0.00	1
175	307210830	08180763-6818468	5271055243163629056	08 18 07.90	−69 41 07.80	10.60	2.51	94.14 ± 0.03	1.1	0.00	3
824	193641523	14483982-5735175	5880886001621564928	14 48 39.72	−58 24 39.96	10.72	1.36	15.61 ± 0.03	1.1	0.02	1
133	219338557	23373497-5857166	6489346046933733632	23 37 35.38	−59 02 41.64	10.72	1.53	20.53 ± 0.03	1.0	0.00	1
1130	254113311	19053021-4126151	6715688452614516736	19 05 30.24	−42 33 44.64	10.88	1.55	17.14 ± 0.05	1.1	0.01	2
198	12421862	00090428-2707196	2333676738049780352	00 09 05.16	−28 52 41.88	10.92	1.99	42.12 ± 0.05	1.0	0.00	1
833	362249359	09423526-6228346	5250780970316845696	09 42 34.92	−63 31 26.76	11.05	1.83	23.94 ± 0.02	0.8	0.01	1
178	251848941	00291228-3027133	2318295979126499200	00 29 12.48	−31 32 45.24	11.15	1.49	15.92 ± 0.05	1.2	0.00	3
279	122613513	02444524-3212391	5063070558501465856	02 44 45.24	−33 47 20.40	11.20	1.44	13.42 ± 0.04	1.1	0.00	1
704	260004324	06042035-5518468	5500061456275483776	06 04 21.60	−56 41 18.60	11.23	2.22	33.48 ± 0.03	1.0	0.00	1
1078	370133522	20274210-5627262	6468968316900356736	20 27 42.86	−57 32 15.72	11.24	2.32	49.06 ± 0.05	1.0	0.00	1
969	280437559	07403284+0205561	3087206553745290624	07 40 32.81	+2 05 54.96	11.25	1.47	12.92 ± 0.05	1.4	0.01	1
620	296739893	09284158-1209551	5738284016370287616	09 28 41.62	−13 49 58.08	11.31	2.24	30.25 ± 0.05	1.0	0.00	1
910	369327947	19205439-8233170	6347634496607835520	19 20 57.10	−83 26 24.72	11.42	2.73	80.09 ± 0.04	1.1	0.00	1
713	167600516	06480517-6537252	5285060409961261696	06 48 05.14	−66 22 32.52	11.42	1.52	14.39 ± 0.02	0.9	0.01	2
932	260417932	06234590-5434414	5499671713762981248	06 23 45.82	−55 25 19.20	11.42	1.41	11.68 ± 0.02	0.8	0.01	2
240	101948569	00590112-4409389	4982951791883929472	00 59 01.18	−45 50 20.76	11.43	1.50	13.33 ± 0.03	1.1	0.00	1
696	77156829	04324261-3947112	4864160624337973248	04 32 42.96	−40 12 32.76	11.54	2.28	50.28 ± 0.02	1.1	0.00	2
244	118327550	00421695-3643053	5001098681543159040	00 42 16.75	−37 16 55.20	11.55	2.55	45.36 ± 0.07	1.3	0.00	1
270	259377017	04333970-5157222	4781196115469953024	04 33 39.86	−52 02 33.36	11.63	2.33	44.46 ± 0.03	1.0	0.00	3
912	406941612	15172165-8028225	5772442647192375808	15 17 18.86	−81 31 36.12	11.64	2.40	38.27 ± 0.02	1.1	0.01	1
475	100608026	05465951-3231592	2901089987127041920	05 46 59.59	−33 28 03.00	11.70	1.76	16.99 ± 0.02	1.0	0.01	1
442	70899085	04164560-1205023	3189306030970782208	04 16 45.65	−13 54 54.36	11.73	1.99	18.98 ± 0.04	1.2	0.00	1
761	165317334	11570326-3806169	3460168250866990848	11 57 03.12	−39 53 42.72	11.73	1.73	14.94 ± 0.04	1.2	0.01	1
870	219229644	04131645-5056400	4782093729275660160	04 13 16.63	−51 03 20.52	11.78	1.99	18.56 ± 0.02	1.1	0.00	1
904	261257684	05572938-8307486	4620844400530949376	05 57 29.11	−84 52 13.08	11.84	2.02	21.67 ± 0.02	1.0	0.01	1
732	36724087	10183516-1142599	3767281845873242112	10 18 34.78	−12 16 55.92	11.85	2.69	45.46 ± 0.08	1.1	0.00	2
656	36734222	10193800-0948225	3767805209112436736	10 19 37.97	−10 11 36.96	11.89	1.63	11.50 ± 0.04	1.1	0.01	1
1075	351601843	20395334-6526579	6426188308031756288	20 39 53.09	−66 33 01.08	12.05	1.84	16.24 ± 0.02	1.2	0.00	1
700	150428135	06282325-6534456	5284517766615492736	06 28 22.97	−66 25 17.04	12.06	2.39	32.10 ± 0.02	1.1	0.00	3
727	149788158	08425684-0229529	3072157538091829120	08 42 56.86	−3 30 05.04	12.07	2.15	23.24 ± 0.03	1.1	0.00	1
249	179985715	00561930-3856552	4987729474846997248	00 56 19.20	−39 03 02.88	12.08	1.70	14.13 ± 0.03	1.1	0.00	1
1201	29960110	02485926-1432152	5157183324996790272	02 48 59.45	−15 27 45.72	12.10	2.37	26.37 ± 0.04	1.1	0.00	1

Table 1 – *continued*

TOI[a]	TIC[b]	2MASS[c]	*Gaia* DR2[d]	RA[d] (hh mm ss.ss)	Dec.[d] (dd mm ss.ss)	G^d (mag)	$B_p - R_p{}^d$ (mag)	Plx[d] (mas)	RUWE[d]	$E(B-V)$	$N^e_{\rm pc}$
875	14165625	05120890-3742313	4820828591913853696	05 12 08.93	−38 17 29.40	12.12	1.51	9.39 ± 0.02	1.0	0.01	1
929	175532955	03033741-3955515	5044287532642519680	03 03 37.73	−40 04 09.12	12.13	1.42	8.71 ± 0.02	1.1	0.01	1
493	19025965	07583071+1253005	3151371883379694720	07 58 30.65	+12 52 59.88	12.19	1.56	9.29 ± 0.04	1.1	0.01	1
1216	141527965	05505139-7541200	4648441970589471104	05 50 51.55	−76 18 41.04	12.31	1.62	10.02 ± 0.03	1.2	0.01	1
233	415969908	22545039-1854426	2402715141877299584	22 54 50.06	−19 05 15.36	12.41	2.27	29.58 ± 0.04	1.0	0.00	2
711	38510224	04100386-6156326	4676789514954240768	04 10 03.86	−62 03 26.28	12.45	1.45	8.43 ± 0.02	1.0	0.01	1
876	32497972	05362611-2414377	2963392606627366912	05 36 26.23	−25 45 20.16	12.47	1.87	12.76 ± 0.03	1.1	0.01	1
785	374829238	05532099-6538022	4755884700667639296	05 53 20.95	−66 21 59.40	12.51	2.04	15.23 ± 0.02	1.0	0.01	1
406	153065527	03170297-4214323	4851053999056603904	03 17 03.02	−43 45 21.24	12.55	2.71	32.17 ± 0.04	1.2	0.00	2
714	219195044	06093401-5349245	5500474185452572032	06 09 34.18	−54 10 37.20	12.56	2.04	18.54 ± 0.02	1.2	0.01	2
900	210873792	16233735-3122228	6037266684232926208	16 23 37.22	−32 37 35.04	12.59	1.52	8.23 ± 0.05	0.9	0.03	1
557	55488511	03560411-1016192	3193508849745633280	03 56 04.27	−11 43 40.80	12.60	1.92	13.14 ± 0.04	1.1	0.01	1
864	231728511	05254662-5121253	4772266186971169792	05 25 46.42	−52 38 34.80	12.66	2.42	26.22 ± 0.03	1.1	0.01	1
256	92226327	00445930-1516166	2371032916186181760	00 44 59.66	−16 43 33.24	12.67	3.04	66.70 ± 0.07	1.1	0.00	2
702	237914496	03444203-6511567	4672700190692201088	03 44 41.98	−66 48 06.12	12.68	1.80	11.82 ± 0.03	1.1	0.01	1
1082	261108236	05330624-8048563	4621526273835900288	05 33 06.19	−81 11 04.20	12.68	1.70	9.95 ± 0.03	1.1	0.01	1
672	151825527	11115769-3919400	5396580575830873728	11 11 57.82	−40 40 18.84	12.72	2.13	14.92 ± 0.03	1.1	0.01	1
806	33831980	04134003-7605515	4627952094666051072	04 13 39.86	−77 54 07.20	12.77	1.67	9.55 ± 0.02	1.3	0.01	1
797	271596225	07141480-7436089	5262540590756812032	07 14 15.14	−75 23 48.84	12.78	2.20	17.77 ± 0.02	1.1	0.01	2
663	54962195	10401596-0830385	3762515188088861184	10 40 15.82	−9 29 20.04	12.81	2.13	15.54 ± 0.04	1.0	0.01	2
540	200322593	05051443-4756154	4785886941312921344	05 05 14.33	−48 03 45.00	12.89	3.11	71.39 ± 0.04	1.0	0.00	1
285	220459976	04584731-5623385	4764216563561182336	04 58 47.33	−57 36 22.32	13.07	1.79	8.61 ± 0.02	0.9	0.01	1
674	158588995	10582099-3651292	5400949450924312576	10 58 20.78	−37 08 30.84	13.08	2.53	21.67 ± 0.05	1.5	0.01	1
789	300710077	07410444-7118157	5264306681309492864	07 41 04.85	−72 41 46.32	13.15	2.44	23.01 ± 0.03	1.3	0.01	1
873	237920046	03465622-6320142	4673392195823039744	03 46 56.78	−64 39 47.16	13.16	2.09	12.97 ± 0.02	1.3	0.01	1
698	141527579	05505661-7637132	4647922867959139072	05 50 57.38	−77 22 49.44	13.26	2.33	15.75 ± 0.03	1.2	0.01	1
136	410153553	22415815-6910089	6385548541499112448	22 41 59.09	−70 49 40.44	13.39	3.40	67.15 ± 0.05	1.1	0.00	1
269	220479565	05032306-5410378	4770828304936109056	05 03 23.11	−55 49 20.28	13.41	2.30	17.51 ± 0.02	1.1	0.01	1
654	35009898	10585379-0532468	3788670679927991296	10 58 53.90	−6 27 09.00	13.42	2.51	17.29 ± 0.05	1.1	0.01	1
782	429358906	12154108-1854365	3518374197418907648	12 15 40.90	−19 05 22.92	13.55	2.71	19.01 ± 0.07	1.2	0.01	1
521	27649847	08132251+1213181	649852779797683968	08 13 22.63	+12 13 19.56	13.58	2.44	16.38 ± 0.06	1.3	0.00	1
203	259962054	02520450-6741155	4647534190597951232	02 52 04.34	−68 18 46.80	13.59	2.94	40.31 ± 0.05	1.4	0.00	1
532	144700903	05401918+1133463	3340265717587057536	05 40 19.22	+11 33 45.36	13.63	1.93	7.38 ± 0.03	1.1	0.02	1
756	73649615	12482523-4528140	6129327525817451648	12 48 24.89	−46 31 46.20	13.66	2.31	11.58 ± 0.04	1.2	0.02	1
302	229111835	01095538-5214219	4927215760764862976	01 09 55.51	−53 45 37.80	13.71	1.64	5.10 ± 0.01	1.0	0.01	1
435	44647437	03573850-2511238	5082797618168232320	03 57 38.54	−26 48 36.36	13.75	1.73	6.02 ± 0.02	1.1	0.01	1
1067	201642601	19144126-5934458	6638412919991750912	19 14 41.28	−60 25 14.16	13.82	1.43	3.76 ± 0.02	1.0	0.03	1
210	141608198	05555049-7359046	4650160717726370816	05 55 50.83	−74 00 52.92	13.84	2.83	23.33 ± 0.05	1.3	0.01	1
1073	158297421	19095625-4939538	6658373007402886400	19 09 56.26	−50 20 06.36	14.31	1.43	3.30 ± 0.04	1.0	0.04	1
468	33521996	05523523-1901539	2966680597368750720	05 52 35.23	−20 58 06.24	14.34	2.01	5.88 ± 0.04	1.2	0.01	1
122	231702397	22114728-5856422	6411096106487783296	22 11 47.57	−59 03 14.04	14.34	2.64	16.07 ± 0.06	1.2	0.00	1
507	348538431	08063103-1545526	5724250571514167424	08 06 31.10	−16 14 07.08	14.48	2.69	8.99 ± 0.06	1.3	0.01	1
551	192826603	05305145-3637508	4821739369794767744	05 30 51.41	−37 22 08.40	14.83	1.84	4.56 ± 0.02	1.0	0.02	1
552	44737596	04034783-2524320	5082914338199586560	04 03 47.86	−26 35 27.96	14.87	2.15	5.10 ± 0.03	1.1	0.01	1
234	12423815	00101648-2616566	2335244779070099200	00 10 16.54	−27 43 03.36	15.69	2.17	3.98 ± 0.07	1.1	0.01	1
555	170849515	04412154-3219128	4877426575724467456	04 41 21.55	−33 40 46.56	15.71	1.80	2.56 ± 0.04	1.0	0.04	1
142	425934411	00182539-6250523	4901321849613348736	00 18 25.42	−63 09 07.56	15.77	2.16	3.09 ± 0.04	1.0	0.01	1

Note.[a] *TESS* Object of Interest ID, [b] *TESS* Input Catalogue ID (Stassun et al. 2018, 2019),[c]2MASS (Skrutskie et al. 2006), [c] *Gaia* (Brown et al. 2018) – note that *Gaia* parallaxes listed here have been corrected for the zero-point offset, [d]Number of candidate planets, NASA Exoplanet Follow-up Observing Program for *TESS*.

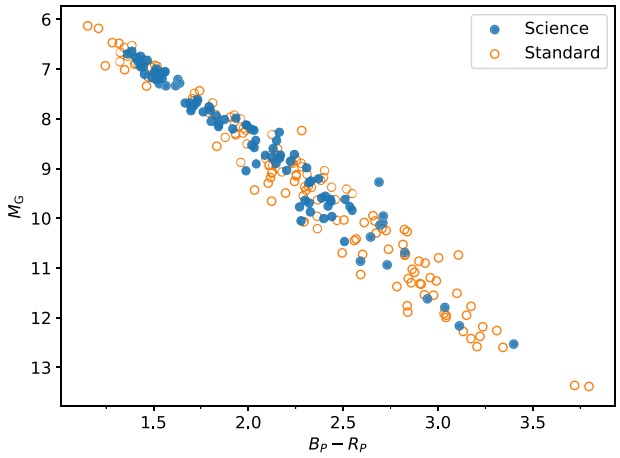

Figure 1. *Gaia* DR2 M_G versus $(B_p - R_p)$ colour–magnitude diagram for science targets (filled blue circles) and cool dwarf standards (orange open circles).

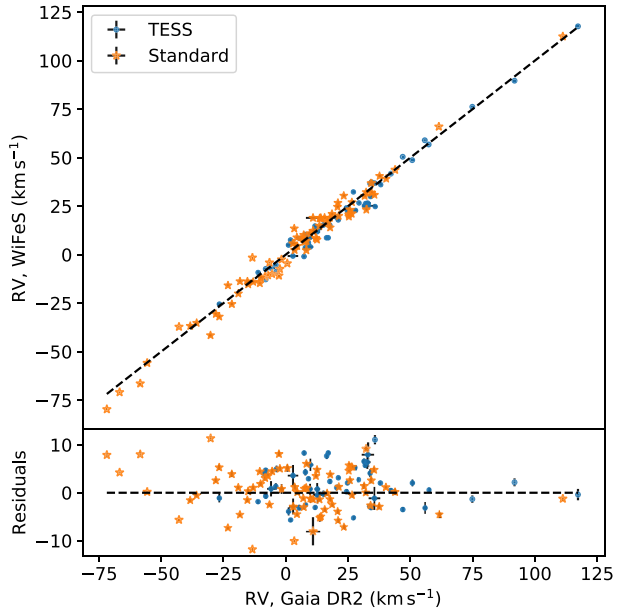

Figure 2. Comparison between those stars with radial velocities in *Gaia* DR2 and our work here, from which we determine a scatter of ∼4.5 km s^{-1}.

or below the mean main sequence is directly correlated with its chemical composition (Baraffe et al. 1998).

These relations are benchmarked on what is considered the gold standard for M-dwarf metallicites: [Fe/H] from a hotter FGK companion taken to have formed at the same time and thus have the same chemical composition. This chemical homogeneity is now well established for FGK–FGK pairs (e.g. Desidera et al. 2004; Hawkins et al. 2020). The process of determining which stars on the sky are likely associated has now been greatly simplified with the release of *Gaia* DR2, which has provided precision parallax measurements and proper motions for nearly all nearby M-dwarfs, with our sample of secondaries having median 0.17 per cent parallax precision.

We take as input the sample of FGK–KM-dwarf pairs compiled by Mann et al. (2013a) and Newton et al. (2014). These combine primary star [Fe/H] measurements from high-resolution spectra sourced from a variety of previous surveys (Mishenina et al. 2004; Luck & Heiter 2005; Valenti & Fischer 2005; Bean et al. 2006a; Ramírez, Allende Prieto & Lambert 2007; Robinson et al. 2007; Fuhrmann 2008; Casagrande et al. 2011; da Silva, Milone & Reddy 2011; Mann et al. 2013a), with Mann et al. (2013a) correcting for inter-survey systematics to place them on a common [Fe/H] scale. To this set, we add the metal-poor, cool subdwarf VB12 to extend our metallicity coverage, taking the [Fe/H] reported by Ramírez et al. (2007) for its primary HD 219617 AB (and correcting for the systematic reported by Mann et al. 2013a). This provided 128 total pairs, which were reduced to 69 after cross-matching with both *Gaia* DR2 and 2MASS, and removing those stars with missing or poor photometry (2MASS Qflg≠'AAA', where 'AAA' is the highest photometric quality rating and corresponds to JHK_S, respectively); those flagged on SIMBAD[6] as spectroscopic binaries; those with poor *Gaia* astrometry (Gaia dup flag=1, RUWE >1.4); those pairs with M dwarf primaries; or whose parallaxes, astrometry, and RVs indicate they are not associated with the putative primary. These 69 stars are listed in Table C1, and span $-1.28 <$ [Fe/H] $< +0.56$.

From this sample, we follow the approaches of Johnson & Apps (2009) and Schlaufman & Laughlin (2010) and use a polynomial to trace the mean main sequence in M_{K_S}−colour space, though using $(B_P - K_S)$ instead of $(V - K_S)$. For our main sequence fit, we use the complete Mann et al. (2015) sample of cool dwarfs with *Gaia* parallaxes, which spans a wider range in $(B_P - K_S)$ and is less sparse than the assembled sample of M-dwarf secondaries. We find the following third-order polynomial sufficient to describe the main sequence:

$$(B_P - K_S) = a_3 M_{K_S}^3 + a_2 M_{K_S}^2 + a_1 M_{K_S} + a_0, \quad (1)$$

where $a_3 = 0.053\ 85$, $a_2 = -1.083\ 56$, $a_1 = 7.761\ 75$, and $a_0 = -14.547\ 05$. We then calculate the offset in $(B_P - K_S)$ from this polynomial (as a colour offers greater discriminatory power than M_{K_S}; Schlaufman & Laughlin 2010), and use least squares to find the best-fitting linear relation for [Fe/H]:

$$[\mathrm{Fe/H}] = b_1 \Delta(B_P - K_S) + b_0, \quad (2)$$

where b_1 and b_0 are the linear polynomial coefficients. After correcting for a remaining trend in the residuals, our adopted coefficients are $b_1 = 0.713\ 39$, and $b_0 = -0.043\ 01$. This relation is valid for stars with $1.51 < (B_P - R_P) < 3.3$ (based on the hottest and coolest secondaries, respectively), and has an uncertainty of ±0.19 dex (from the standard deviation in the residuals). We stress that the relation should only be used for stars that pass the same quality cuts we use to build the relation: unsaturated photometry, not flagged as a duplicate source in *Gaia*, RUWE <1.4, and not a known/suspected spectroscopic binary or pre-main-sequence star. Our [Fe/H] recovery and fits can be seen in Fig. 3.

4 SPECTROSCOPIC ANALYSIS

The *TESS* candidate planet host observing programme described here developed from an ANU 2.3 m/WiFeS survey of potential young stars (Žerjal et al. 2021) to identify signs of youth (via Balmer Series and Ca II H&K emission, and Li 6708 Å absorption) and determine RVs to enable kinematic analysis with `Chronostar` (Crundall et al. 2019) when combined with *Gaia* astrometry. While their spectral type coverage ($1.27 < B_P < 2.6$) was relatively similar to our own, instrument set-up, however, prioritized higher spectral resolution for

[6]http://simbad.u-strasbg.fr/simbad/

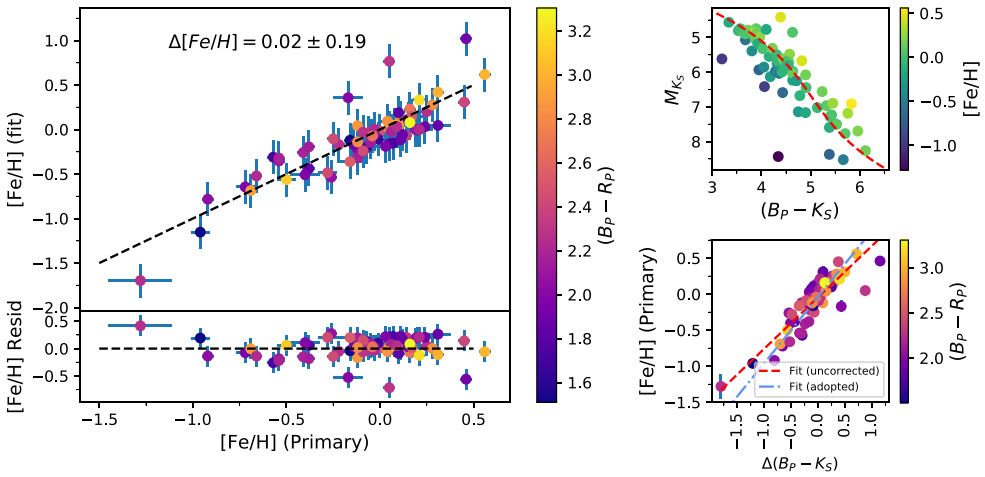

Figure 3. *Left:* Cool dwarf secondary [Fe/H] calculated from our photometric calibration versus [Fe/H] from the associated FGK primary star, colour coded by *Gaia* $(B_P - R_P)$. The standard deviation of the residuals, and our adopted uncertainty for the relation, is ±0.19 dex. See Table C1 for further information on this FGK–KM binary calibration sample. *Top Right:* $M_{K_S} - (B_P - K_S)$ colour–magnitude diagram for the calibration sample of cool dwarf secondaries colour coded by host star [Fe/H]. The dashed red line is a third-order polynomial representing the main sequence, fitted to the Mann et al. (2015) sample of cool dwarfs. *Bottom right:* Fitted [Fe/H] as a function $\Delta(B_P - K_S)$ offset from the mean main sequence polynomial. The dashed red line is the initial uncorrected linear least-squares fit, and the dash–dotted blue line is the adopted fit after correcting for the remaining trend in the residuals.

improved velocity precision and coverage of the key wavelength regions of interest. These regions are firmly in the optical, where M-dwarf spectral features are strongly blended and heavily dominated by molecular absorption from hydrides (e.g. MgH, CaH, and SiH) and oxides (e.g. TiO, VO, and ZrO). This is in contrast to most of the previous low–medium resolution studies of M-dwarfs that work in the NIR where the absorption is less severe and many more [Fe/H] sensitive features are available.

Here, we describe our attempts to derive reliable atmospheric parameters from our spectra using a model-based approach. Our investigation ultimately revealed substantial systematics and degeneracies when fitting to model optical spectra, resulting in our inability to recover $\log g$ or [Fe/H]. While the spectra are included in our temperature fitting routine, they are primarily used for RV determination, identification of peculiarities (such as signs of youth), and for testing model fluxes. The details of our findings are covered below, and we await follow-up work to explore a standard-based or data-driven approach (e.g. similar to the work of Birky et al. 2020, but in the optical) to take full advantage of the information in our now large library of optical cool dwarf spectra.

4.1 Selection of model atmosphere grid

While synthetic spectra show better agreement for FGK stars, the onset of strong molecular features such as TiO and H_2O in the atmospheres of late K and M dwarf atmospheres makes the task of modelling their spectra far more complex. There are known historical issues, for instance, when computing optical colours from synthetic spectra (e.g. difficulties in computing accurate *V*-band magnitudes; Leggett et al. 1996), and the line lists required are considerably more complicated. Thus, before using models in our automatic fitting routine, we first investigate their performance at different wavelengths to flag regions requiring special consideration. For the purposes of this comparison, we check the MARCS grid of stellar atmospheres against the BT-Settl grid (Allard, Homeier & Freytag 2011), both of which are described in detail below.

Our template grid of 1D LTE MARCS spectra was previously described by Nordlander et al. (2019) and computed using the TURBOSPECTRUM code (v15.1; Alvarez & Plez 1998; Plez 2012) and MARCS model atmospheres (Gustafsson et al. 2008). The spectra are computed with a sampling resolution of 1 km s^{-1}, corresponding to a resolving power of $R \sim 300\,000$, with a microturbulent velocity of 1 km s^{-1}. We adopt the solar chemical composition and isotopic ratios from Asplund et al. (2009), except for an alpha enhancement that varies linearly from $[\alpha/\mathrm{Fe}] = 0$ when $[\mathrm{Fe/H}] \geq 0$ to $[\alpha/\mathrm{Fe}] = +0.4$ when $[\mathrm{Fe/H}] \leq -1$. We use a selection of atomic lines from VALD3 (Ryabchikova et al. 2015) together with roughly 15 million molecular lines representing 18 different molecules, the most important of which for this work are CaH (Plez, priv. comm.), MgH (Kurucz 1995; Skory et al. 2003), and TiO (with updates via VALD3 Plez 1998).

MARCS model fluxes were developed for usage over a range of spectral types including both cool giants and, critically for our work here, cool dwarfs. Recent work fitting cool dwarf stellar atmospheres, however, have mostly used high-resolution NIR spectra (*J* band: Önehag et al. 2012; Lindgren, Heiter & Seifahrt 2016; Lindgren & Heiter 2017; *H* band: Souto et al. 2017, 2018) rather than the medium-resolution optical spectra we use here.

For BT-Settl, we use the most recently published grid (Allard, Homeier & Freytag 2012a; Allard et al. 2012b; Baraffe et al. 2015)[7] that uses abundances from Caffau et al. (2011) and covers $1200 < T_{\mathrm{eff}} < 7000$ K, $2.5 < \log g < 5.5$, and [M/H]=0.0. Note that while older grids have a wider range of [M/H], they are also less complete in terms of physics and line lists, so we opt for the newest grid for our comparison here, and limit ourselves to testing on stars with approximately solar [Fe/H].

BT-Settl atmospheres have been developed with a focus on cool dwarf atmospheres and have a strong history of use for studying cool dwarfs at a variety of wavelengths and resolutions (e.g. Mann et al. 2012, 2013c, 2015; Muirhead et al. 2012; Rojas-Ayala et al.

[7] https://phoenix.ens-lyon.fr/Grids/BT-Settl/CIFIST2011_2015/

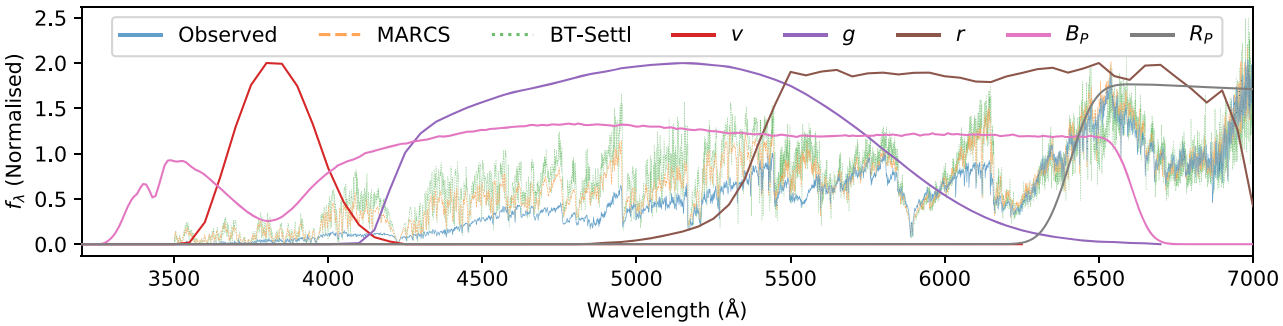

Figure 4. Observed WiFeS B3000 and R7000 spectra for GJ 447, along with a MARCS synthetic spectrum interpolated to the parameters from Mann et al. (2015) ($T_{\rm eff}$ = 3192 K, log g = 5.04, [Fe/H] = −0.02), and a PHOENIX/BT-Settl spectrum at the closest grid point available ($T_{\rm eff}$ = 3200 K, log g = 5.0, [Fe/H] = 0.0). SkyMapper v, g, r, and *Gaia* B_P and R_P filters are overplotted for reference. Note the severe model disagreement below 5400 Å.

2012; Lépine et al. 2013; Rajpurohit et al. 2013; Gaidos et al. 2014; Veyette et al. 2016, 2017; Souto et al. 2018). Most noteworthy for our comparison are tests by Reylé et al. (2011) and Mann et al. (2013c), which examined model performance at optical wavelength regions >5500 Å common to our WiFeS R7000 spectra.

For each of our standard stars, we combined and normalized our flux-calibrated B3000 and R7000 spectra to give a single spectrum with 3500 Å < λ < 7000 Å. To this we compared synthetic MARCS fluxes interpolated to literature values of $T_{\rm eff}$, log g, and [Fe/H], as well as the BT-Settl equivalent for those with close to solar [Fe/H]. Given our large library of standards, we were able to observe model performance as a function of both stellar parameters and wavelength. A representative comparison (with overplotted filter bandpasses) is shown in Fig. 4, and our main conclusions are summarized as follows:

(i) Both MARCS and BT-Settl models severely overpredict (worsening with decreasing $T_{\rm eff}$) flux bluewards of ∼5400 Å. The MARCS systematic offset is also a strong function of [Fe/H], an effect also observed in Joyce & Chaboyer (2015), and while this is likely also true for BT-Settl, we cannot comment definitively while limited to the solar [Fe/H] grid.

(ii) BT-Settl additionally underpredicts flux at ∼6500 Å (as expected from Reylé et al. 2011 and Mann et al. 2013c).

(iii) Synthetic photometry generated in SkyMapper v, g, r, and *Gaia* B_P is thus systematically brighter than the observed equivalents for reasonable assumptions of $T_{\rm eff}$, log g, and [Fe/H] for the star under consideration.

We are able to quantify these systematics by integrating photometry from our flux-calibrated observed spectra and comparing to the MARCS synthetic equivalents generated at the literature parameters for each star. Our wavelength coverage allows us to check the magnitude offsets Δv, Δg, Δr, and ΔB_P, corresponding to v, g, r, and B_P, respectively. We note that for the purpose of this comparison we do not account for inaccuracies in our flux calibration, telluric absorption, nor for WiFeS not covering the bluest ∼200 Å of B_P. However, checks with synthetic spectra show that this region accounts for less than 0.25 per cent of B_P flux at 3000 K where our correction is greatest, and remains less than 0.5 per cent of flux at 4500 K where our correction is more modest. These offsets are shown for g, r, and B_P in Fig. 5, and fit separately for each filter by the following linear relation in observed *Gaia* DR2 ($B_P - R_P$):

$$\Delta m_\zeta = a_1(B_P - R_P) + a_0, \quad (3)$$

where Δm_ζ is the magnitude offset in filter ζ; a_1 equals 0.116, 0.084, and 0.034 for g, r, and B_P fits, respectively; and a_0 equals

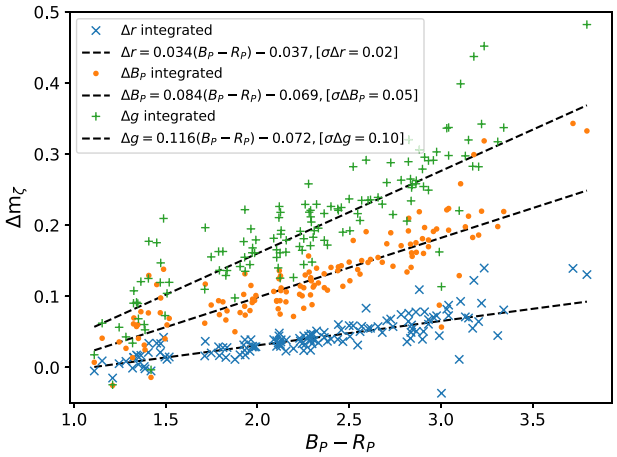

Figure 5. *Gaia* B_P, and SkyMapper gr systematic offsets between integrated flux-calibrated WiFeS spectra and MARCS model integrated spectra at literature parameters for our standard stars, plotted as a function of observed *Gaia* $B_P - R_P$. Stars redder in $B_P - R_P$ have systematically more flux at bluer wavelengths, with the best-fitting linear magnitude offset plotted for each filter, and the standard deviation in magnitude noted.

−0.072, −0.069, and −0.037 for g, r, and B_P fits, respectively. Computing the standard deviation for the residuals shows 0.10, 0.05, and 0.02 uncertainties in magnitude (equivalent to roughly 10 per cent, 5 per cent, and 2 per cent uncertainties in flux) for g, r, and B_P, respectively. From this, we conclude that while the corrections to r, and B_P, are modest, g is likely too affected to prove useful.

Following this both qualitative and quantitative investigation comparing model fluxes to our library of standard star spectra, we make the following decisions for our synthetic fitting methodology:

(i) Given similar observed systematics for both MARCS and BT-Settl model fluxes, we adopt the MARCS grid to enable fitting for [Fe/H] as well as $T_{\rm eff}$ and log g.

(ii) Only use our R7000 spectra (5400 Å ≤ λ ≤ 7000 Å) for fitting, additionally masking out the two regions worst affected by missing opacities (5498–5585 Å and 6029–6159 Å).

(iii) Apply an *observed* ($B_P - R_P$)-dependent systematic offset to our generated synthetic B_P and r photometry per equation (3).

(iv) Given the widespread historical use and success of studying M-dwarfs at NIR wavelengths, we use R_P, i, z, J, H, and K_S photometry assuming no substantial model systematics.

(v) However, to account for remaining model uncertainties, we add conservative ±0.011 mag (1 per cent in flux) uncertainties in quadrature with the observed uncertainties for R_P, i, z, and the fitted ±0.02 for r, and ±0.05 for B_P.

4.2 Synthetic fitting

Our approach to spectral fitting was developed specifically to work with the complicated spectra of our cool star sample and incorporates nine distinct sources of information. While it was hoped that this methodology would be sufficient to disentangle the strong degeneracy between $T_{\rm eff}$ and [Fe/H] and accurately recover *distant-independent* [Fe/H] for our standard sample, this ultimately proved not to be the case. While we are able to tightly constrain $T_{\rm eff}$, we must resort to using the photometric [Fe/H] relation developed in Section 3 to fix [Fe/H] during the fit. The information included in our fit is as follows:

(i) medium-resolution R7000 optical spectra from WiFeS,
(ii) observed *Gaia* B_P, R_P; 2MASS J, H, and K_S; and SkyMapper DR3 r, i, z photometry,
(iii) empirical cool dwarf radius relations from Mann et al. (2015) – valid for K7–M7 stars, and used to estimate $\log g$,
(iv) empirical cool dwarf mass relations from Mann et al. (2019) – valid for $0.075\,{\rm M}_\odot < M_\star < 0.70\,{\rm M}_\odot$, and used to estimate $\log g$,
(v) synthetic MARCS model spectra (for spectral fitting, interpolated to the resolution and wavelength grid of WiFeS)
(vi) MARCS model fluxes (for photometric fitting),
(vii) stellar parallaxes from *Gaia* DR2,
(viii) the interstellar dust map from Leike & Enßlin (2019),
(ix) a set of reference stellar standards with known parameters for testing and validation purposes (see Section B for details).

We found that least-squares fitting between real and synthetic spectra alone consistently underestimated expected $\log g$ values of our sample by up to 0.3 dex – physical for a set of young stars, but not realistic for our overwhelmingly main sequence sample. To counter this, we calculate $\log g$ using the absolute K_S-band radius and mass relations of Mann et al. (2015, 2019),[8] respectively, and fix it during fitting. We then use a two-step iterative procedure, with the first fit fixing $\log g$ to the value from empirical relations, and a second and final fit using our interim-measured radius and a mass from Mann et al. (2019). All of our *TESS* targets fall within the stated $4 < M_{K_S} < 11$ limits for the mass relation. Although the relation is only valid for main-sequence stars, we employ it with caution for two suspected young stars TOI 507 (TIC 348538431) and TOI 142 (425934411), both discussed in more detail in Section 6.5, on the assumption that the resulting value of $\log g$ will still be more accurate than an unconstrained synthetic fit. Additionally, we suspect TOI 507 of being a near-equal mass binary, and as such treat it as 0.75 mag fainter (or half as bright) for the purpose of using the relation, equivalent to determining the mass for only a single component.

While this now solves the $\log g$ issue, we are still left with two issues arising from the spectra themselves. The first is that certain wavelength regions of our MARCS model spectra are a poor match compared to our reference sample with known $T_{\rm eff}$, $\log g$, and [Fe/H] – particularly at cooler temperatures. As discussed in Section 4.1, we account for this by using only spectra from the red arm of WiFeS with $\lambda > 5400$ A, and masking out remaining regions with poor agreement.

The second remaining issue is that of the degeneracy between $T_{\rm eff}$ and [Fe/H] when fitting spectra. This effect is caused by both the temperature and metallicity influencing the strength of atmospheric molecular absorbers or opacity sources (predominantly TiO in the optical, but also various hydrides). What this means in practice is that there often is not a single minimum or optimal set of atmospheric parameters when fitting synthetic spectra, but instead there exists a range of good fits (or even multiple minima) at different combinations of $T_{\rm eff}$ and [Fe/H] – possibly separated by several 100 K in $T_{\rm eff}$ or several 0.1 dex in [Fe/H].

In an attempt to overcome this, we include photometry from redder wavelengths that are less dominated by absorption than optical wavelengths, meaning that $T_{\rm eff}$ and [Fe/H] are less degenerate. While we do not have NIR spectra for our science or reference sample, we do have *Gaia*, SkyMapper, and 2MASS photometry in the form of B_P, R_P, r, i, z, J, H, and K_S that together give us almost continuous wavelength coverage out to nearly 2.4 μm and covers the bulk of stellar emission for our cool stars.

We thus modified our fitting methodology to also compute the uncertainty weighted residuals between observed and synthetic stellar photometry. In order to compare synthetic photometry to its observed equivalent, we formulate the fit as follows:

$$m_{\zeta,m} = {\rm BC}_\zeta(T_{\rm eff}, \log g, [{\rm Fe/H}]) + m_{\rm bol}, \tag{4}$$

where $m_{\zeta,m}$ is the model magnitude in filter ζ; ${\rm BC}_\zeta$ is the bolometric correction (i.e. the total flux outside of a filter ζ) as a function of $T_{\rm eff}$, $\log g$, and [Fe/H] in filter ζ; and $m_{\rm bol}$ is the apparent bolometric magnitude (i.e. the apparent magnitude of the star over all wavelengths). In this implementation, $m_{\rm bol}$ serves as a physically meaningful free parameter used to scale synthetic magnitudes to their observed equivalents and ultimately allow the computation of the apparent bolometric flux $f_{\rm bol}$. This is done using the well-tested BOLOMETRIC-CORRECTIONS[9] software (Casagrande & VandenBerg 2014, 2018a,b) to interpolate a grid of bolometric corrections from MARCS fluxes in different filters for the stellar parameters at each fitting call. By fitting for $m_{\rm bol}$ and using bolometric corrections, we are thus directly able to compare an observed magnitude, $m_{\zeta,o}$, from *Gaia*, SkyMapper, or 2MASS directly with its MARCS synthetic equivalent. With $\log g$ fixed, we now have a three-term fit in terms of $T_{\rm eff}$, [Fe/H], and $m_{\rm bol}$, the latter of which allows for the direct computation of the bolometric flux (and thus the stellar radius).

This fitting procedure is equivalent to minimizing the following relation (performed using the least_squares function from `scipy`'s optimize module):

$$R(\theta) = \sum_{i=1}^{M}\left(\frac{1}{C\sqrt{\chi^2_f}}\frac{f_{o,i}-f_{m,i}}{\sigma_{f_{o,i}}}\right)^2 + \sum_{\zeta=1}^{N}\left(\frac{1}{\sqrt{\chi^2_m}}\frac{m_{\zeta,o}-(m_{\zeta,m}+\Delta m_\zeta)}{\sigma_{m_\zeta}}\right)^2 \tag{5}$$

with model uncertainties taken into account via

$$\sigma_{m_\zeta} = \sqrt{\sigma^2_{m_{\zeta,o}} + \sigma^2_{m_{\zeta,m}}}, \tag{6}$$

where $R(\theta)$ are the combined spectral and photometric squared residuals as a function of θ, a vector of $T_{\rm eff}$, $\log g$, [Fe/H], $m_{\rm bol}$; M is the total number of spectral pixels, i is the spectral pixel index, $f_{\rm o,i}$ and

[8]Calculated using the PYTHON code available at https://github.com/awmann/M_-M_K-.

[9]https://github.com/casaluca/bolometric-corrections

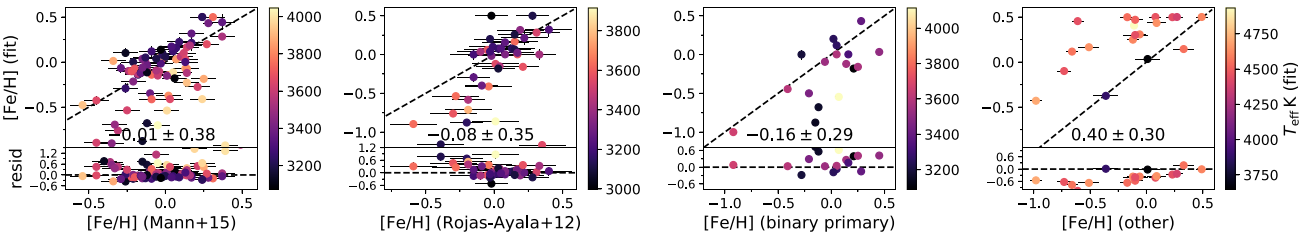

Figure 6. [Fe/H] recovery for our three-parameter fit in $T_{\rm eff}$, [Fe/H], and $m_{\rm bol}$ for our four sets of [Fe/H] standards: Mann et al. (2015), Rojas-Ayala et al. (2012), primary star [Fe/H] for cool dwarfs in binaries, and mid-K dwarfs. The median and standard deviation of each set of residuals are annotated. Note the inability of the three-parameter fit to reliably recover [Fe/H], with the scatter on our recovered [Fe/H] for the binary sample (the most reliable set of [Fe/H] standards) being larger than the scatter on our photometric [Fe/H] relation.

$f_{\rm m,i}$ are the observed and model spectral fluxes, respectively, at pixel i, normalized by their respective medians in the range of 6200 Å $\leq \lambda \leq$ 7000 Å; $\sigma_{f_{\rm o,i}}$ is the observed flux uncertainty at pixel i; N is the total number of photometric filters; ζ is the filter index and $m_{\zeta,o}$ and $m_{\zeta,m}$ are the observed and model magnitudes, respectively, in filter ζ; Δm_ζ is the systematic model magnitude offset in filter ζ (per equation 3 for r and B_P, and 0 for all other filters); $\sigma_{m_{\zeta,o}}$ and $\sigma_{m_{\zeta,m}}$ are the uncertainties on the observed and model magnitudes, respectively, added in quadrature to give the total magnitude uncertainty σ_{m_ζ}; χ^2_f and χ^2_m are the *global* minimum χ^2 values computed from the spectral and photometry residuals, respectively (i.e. global fit using only R7000 spectra, without photometry, and a separate global photometric fit without spectra), used to normalize the two sets of residuals in the case of poor fits and place them on a similar scale; and C, set to 20, is a constant used to account for the spectra having many more pixels than the number of photometric points. This value of C was chosen by visually inspecting the residuals of our spectral fits and means that we assume, on average, every 20 spectral pixels are correlated and do not contain unique information.

We test the accuracy of our fitted [Fe/H] using a set of cool star stellar standards in Fig. 6. It is immediately clear that, despite the tight constraint on $T_{\rm eff}$ that our broad wavelength coverage from photometry allows, we are unable to recover [Fe/H] for our standard sample to better precision than our photometric [Fe/H] relation from Section 3. Our fits systematically overpredict [Fe/H] for the coolest stars in our sample, which might be similar to what was observed in fig. 3 of Rojas-Ayala et al. (2012) (using BT-Settl models), where they find even metal-rich models fail to reproduce the depth of certain features. This has also previously been observed for cool, metal-poor clusters when using evolutionary models (e.g. Joyce & Chaboyer 2015), and observed for isochrones (e.g. Joyce & Chaboyer 2018). From this, we conclude that a simple least-squares fit to our medium-resolution optical spectra, unweighted to [Fe/H] sensitive regions, and using models with both known and unknown systematics is not sufficient to accurately determine [Fe/H] for cool dwarfs.

Given this, it is clear that a three-parameter fit to $T_{\rm eff}$, [Fe/H], and $m_{\rm bol}$ is unreasonable. Our final reported parameters are thus a two-parameter fit to $T_{\rm eff}$, and $m_{\rm bol}$, fixing [Fe/H] to the value from our relation in Section 3 for those stars falling within the ($B_P - R_P$) range, and the mean value for the Solar Neighbourhood of [Fe/H] = −0.14 (Schlaufman & Laughlin 2010) for stars outside this range, or suspected of binarity or being young. To further account for both model and zero-point uncertainties, we add a 1 per cent flux uncertainty in quadrature with our fitted statistical uncertainties on $m_{\rm bol}$. Our standard star $T_{\rm eff}$ recovery for the two-parameter fit is shown in Fig. 7.

We compute the apparent bolometric flux $f_{\rm bol}$ from our fitted value of $m_{\rm bol}$ using equation (3) from Casagrande & VandenBerg (2018a), from which we then compute the stellar radius $R_\star$. Fig. 8 shows a comparison between our radii and those from our interferometric standard sample, and final values for *TESS* science targets and stellar standards are reported in Tables 2 and B2, respectively.

5 CANDIDATE PLANET PARAMETERS

5.1 Transit light-curve analysis

We now present results for all TOIs not ruled out as false positives (e.g. due to background stars, or eclipsing binaries) by the *TESS* team and exoplanet community, as listed on the NASA ExoFOP-*TESS* website.

Transit light curves for targets across all *TESS* sectors were downloaded from NASA's Mikulski Archive for Space Telescopes service. For all high-cadence data, we used the Pre-search Data Conditioning Simple Aperture Photometry (PDCSAP) fluxes, which have already had some measure of processing to remove systematics. All light curves were downloaded and manipulated using the PYTHON package `LightKurve` (Lightkurve Collaboration 2018).

Many stars in our sample show some amount of stellar variability, with periods ranging from days to many weeks. We remove this using `LightKurve`'s flatten function, which applies a Savitzky–Golay filter (Savitzky & Golay 1964) to the data to remove low frequency trends. When applying the filter, we mask out all planetary transits by known TOIs. Once flattened, the light curves are then phase folded using either the period provided by NASA ExoFOP-*TESS* (for most stars), or our own fitted period (for stars revisited in the *TESS* extended mission whose long time baseline reveals the ExoFOP-*TESS* period to be incorrect). We use the provided measurement of transit duration to select only photometry from the transit itself, plus 10 per cent of a duration either side for use in model fitting.

Model fitting is implemented using the PYTHON package `BATMAN` (Kreidberg 2015), which is capable of generating model transit light curves for a given set of orbital elements (scaled by the stellar radius $R_\star$) and limb darkening coefficients. We use a four-term limb darkening law, interpolating the PHOENIX grid provided by Claret (2017) using values of $T_{\rm eff}$ and $\log g$ from Table 2. The resulting coefficients are in Table D1.

Transit photometry alone is not sufficient to uniquely constrain the planet orbit and radius when fitting for the scaled semimajor axis $a_{R_\star} = \frac{a}{R_\star}$, the planetary radius ratio $R_{P,R_\star} = \frac{R_P}{R_\star}$, the inclination i, the eccentricity e, and the longitude of periastron ω (Kipping 2008). While we can use our measurements of $M_\star$, $R_\star$, and T to constrain the semimajor axis of a circular orbit (equation 7), we do not have

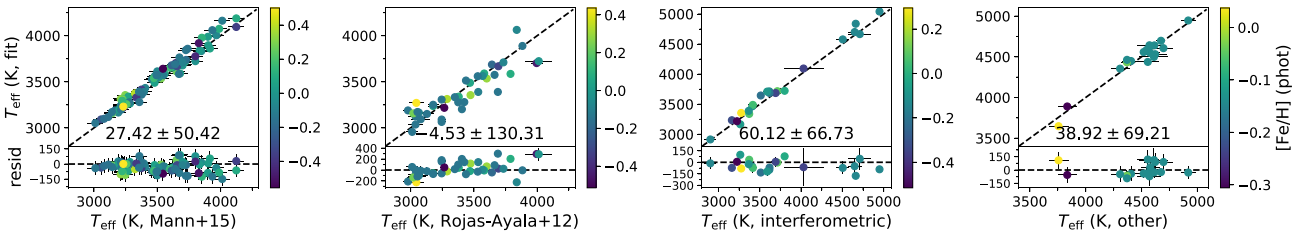

Figure 7. $T_{\rm eff}$ recovery for our two-parameter fit in $T_{\rm eff}$, and $m_{\rm bol}$ for our four sets of $T_{\rm eff}$ standards: Mann et al. (2015), Rojas-Ayala et al. (2012), interferometry, and mid-K dwarfs. [Fe/H] is from our photometric [Fe/H] relation where appropriate, or fixed to the mean Solar Neighbourhood [Fe/H] if not. The median and standard deviation of each set of residuals are annotated (note that these values have not yet been corrected for the systematic, as discussed in Section 6.2).

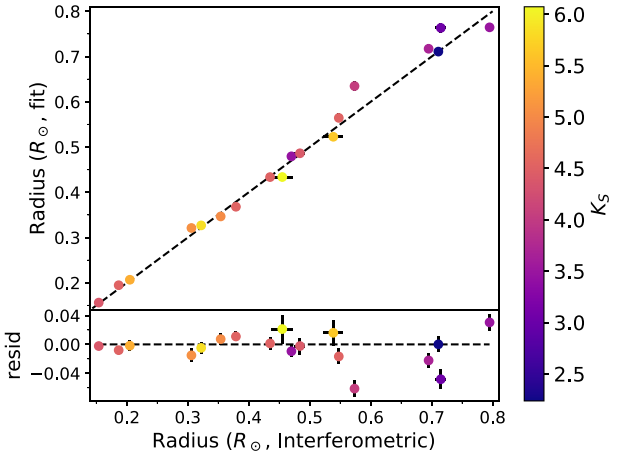

Figure 8. Radius comparison for those targets with interfometric radii to better than 5 per cent precision. The median distance precision for these targets is 0.04 per cent. We find generally good agreement between literature measurements and our own, though noting that the brightness of this sample (see apparent 2MASS K_S magnitude on the colour bar) results in photometry that is either saturated or has lower precision and thus may be the cause of some of the scatter observed.

the precision required to fit for eccentric orbits. As such, we fix $e = 0$ and $\omega = 0$ during our fit, and include our calculated value $a_{R_\star,c}$ – the value $a_{R_\star}$ assuming a circular orbit, as a prior during fitting. In cases where $e \sim 0$, we expect the fitted semimajor axis $a_{R_\star,f}$ to approach $a_{R_\star,c}$. For cases with a discrepancy between the two, we flag the planet as an indication of a possibly eccentric orbit in Table 3.

This measured semimajor axis, calculated using our Mann et al. (2015) absolute K_S-band $M_\star$, and T from NASA ExoFOP, can be constrained as follows:

$$a = \sqrt[3]{\frac{GM_\star T^2}{4\pi^2}}, \tag{7}$$

where a is the semimajor axis, G is the gravitational constant, $M_\star$ is the stellar mass (with $M_\star >> M_{\rm p}$, the planetary mass), and T is the planet orbital period – all of which we assume are independent quantities.

Now with a prior on the semimajor axis, we again use the least_squares function from `scipy`'s optimize module to perform least-squares fitting to minimize the following expression:

$$R_t = \left(\frac{a_{R_\star,m} - a_{R_\star,f}}{\sigma_{a_{R_\star,m}}} + \sum_j^N \frac{t_{\rm obs,\,j} - t_{\rm model,\,j}}{\sigma_{t_{\rm obs,\,j}}} \right)^2, \tag{8}$$

where R_t are the light curve and prior residuals (as a function of $R_{p,R_\star}$, $a_{R_\star,f}$, and i), $a_{R_\star,m}$ is the measured scaled semimajor axis, $a_{R_\star,f}$ is the fitted scaled semimajor axis, $\sigma_{a_{R_\star,m}}$ is the uncertainty on the measured scaled semimajor axis, j is the time-step, N is the total number of epochs, $t_{\rm obs,j}$ is the observed flux at time-step j, $t_{\rm model,j}$ is the model flux at time-step j, and $\sigma_{t_{\rm obs,\,j}}$ is the measured flux uncertainty at time-step j.

Results from this fitting procedure are presented in Table 3, a comparison with confirmed planets in Fig. 11, and a histogram of the resulting planet candidate radii in Fig. 12. Note that we do not fit the light curves for some candidates: TOIs 256.01 and 415969908.02 have only two and one transits respectively; TOI 507.01 is a suspected equal-mass binary; TOIs 302.01 and 969.01 do not have PDCSAP 2 min cadence data; and TOIs 203.01, 253.01, 285.01, 696.02, 785.01, 864.01, 1216.01, 260417932.02, and 98796344.02 have transits observed only at low SNR.

6 DISCUSSION

6.1 Radial velocities

Just over half our *TESS* sample has radial velocities in *Gaia* DR2, with the remaining 42 therefore having an incomplete set of positional and kinematic data. Our RVs are consistent with *Gaia* DR2 for our overlap sample and accurate to within $\sim$4.5 km s^{-1} (Section 2.4), thus providing RVs for the remainder and enabling insight into Galactic population, or kinematic analysis using tools such as `Chronostar` (Crundall et al. 2019) to determine ages for those that are found to be members of stellar associations. These results are especially interesting given the planet-hosting nature of these stars.

6.2 Standard star parameter recovery

Comparing our $T_{\rm eff}$ results to those of Mann et al. (2015) reveals excellent agreement for our two-parameter fit (Fig. 7), with the scatter on our residuals being smaller than their mean reported uncertainty of 60 K and only a relatively small systematic of $\sim$30 K observed. Such consistency is encouraging given that this represents our largest uniform set of comparison stars, a set whose temperatures have already been successfully benchmarked against those from interferometry and should be much less sensitive to model limitations than our own.

When comparing to Rojas-Ayala et al. (2012), the results are less consistent, though we observe a similar effect to Mann et al. (2015) in that Rojas-Ayala et al. (2012) overestimate temperatures for the warmest stars. These temperatures, however, come solely from measurement of the H_2O-K2 index in the K band in conjunction with

Table 2. Final results for *TESS* candidate exoplanet hosts. Full table is available online as supplementary material.

TOI	TIC	$T_{\rm eff}$ (K)	log g	[Fe/H]	M ($M_\odot$)	$R_\star$ ($R_\odot$)	$m_{\rm bol}$	$f_{\rm bol}$ (10^{-12} erg s^{-1} cm^{-2})	EW (H α) (Å)	log $R'_{\rm HK}$
136	410153553	2988 ± 30	5.06 ± 0.02	–	0.155 ± 0.004	0.192 ± 0.004	12.05 ± 0.01	384.4 ± 3.9	−0.05	−5.37
540	200322593	3104 ± 30	5.07 ± 0.02	−0.10	0.164 ± 0.004	0.197 ± 0.004	11.71 ± 0.01	528.3 ± 5.3	2.49	–
256	92226327	3150 ± 30	5.01 ± 0.02	−0.13	0.182 ± 0.005	0.220 ± 0.004	11.55 ± 0.01	611.8 ± 6.1	−0.22	−5.53
203	259962054	3169 ± 30	5.01 ± 0.02	−0.07	0.200 ± 0.005	0.232 ± 0.004	12.49 ± 0.01	255.4 ± 2.6	0.56	−4.98
507	348538431	3279 ± 30	4.76 ± 0.02	–	0.383 ± 0.010	0.424 ± 0.008	14.28 ± 0.01	49.2 ± 0.5	2.24	−4.49
910	369327947	3282 ± 30	4.97 ± 0.02	−0.04	0.262 ± 0.008	0.278 ± 0.005	10.46 ± 0.01	1656.2 ± 16.6	−0.27	−5.47
210	141608198	3284 ± 30	4.90 ± 0.02	0.21	0.312 ± 0.008	0.326 ± 0.006	12.78 ± 0.01	195.8 ± 2.0	−0.23	−5.84
122	231702397	3326 ± 30	4.86 ± 0.02	−0.07	0.316 ± 0.008	0.345 ± 0.006	13.42 ± 0.01	109.3 ± 1.1	−0.21	–
455	98796344	3330 ± 30	4.97 ± 0.02	−0.27	0.248 ± 0.006	0.271 ± 0.005	9.16 ± 0.01	5507.5 ± 54.8	−0.29	−5.39
732	36724087	3354 ± 30	4.83 ± 0.02	0.13	0.364 ± 0.009	0.382 ± 0.007	10.91 ± 0.01	1103.5 ± 11.0	−0.23	−5.55

Table 3. Final results for *TESS* candidate exoplanets. Full table is available online as supplementary material.

TOI	TIC	Sector/s	Period (days)	$R_p/R_\star$	$a/R_\star$	e flag	i (°)	R_p ($R_\oplus$)
122.01	231702397	1, 27–28	5.078 03 †	0.0797 ± 0.0022	24.63 ± 0.49	0	88.337 ± 0.001	3.00 ± 0.10
129.01	201248411	1–2, 28–29	0.980 97 †	0.3223 ± 0.0884	5.15 ± 0.04	0	76.381 ± 0.018	25.35 ± 6.96
133.01	219338557	1, 28	8.199 18 †	0.0269 ± 0.0010	23.15 ± 0.41	0	88.470 ± 0.002	1.88 ± 0.07
134.01	234994474	1, 28	1.401 53 †	0.0223 ± 0.0006	6.98 ± 0.16	0	84.566 ± 0.005	1.54 ± 0.05
136.01	410153553	1, 27–28	0.462 93 †	0.0587 ± 0.0006	6.80 ± 0.17	1	90.000 ± 5.000	1.23 ± 0.03
139.01	62483237	1, 28	11.070 83 †	0.0346 ± 0.0008	27.20 ± 0.56	0	88.549 ± 0.001	2.54 ± 0.07
142.01	425934411	1–2, 28–29	0.853 35 †	0.1809 ± 0.0184	4.74 ± 0.11	0	79.385 ± 0.012	13.31 ± 1.39
175.01	307210830	2, 5, 8–12, 28–29, 32	3.690 66 †	0.0397 ± 0.0003	21.32 ± 0.47	0	88.809 ± 0.002	1.32 ± 0.03
175.02	307210830	2, 5, 8–12, 28–29, 32	7.450 75 †	0.0446 ± 0.0006	34.59 ± 0.75	0	88.483 ± 0.001	1.48 ± 0.03
175.03	307210830	2, 5, 8–12, 28–29, 32	2.253 10 †	0.0238 ± 0.0003	15.76 ± 0.34	0	88.133 ± 0.003	0.79 ± 0.02

Notes. Periods denoted by † are not as reported by ExoFOP, and have been refitted here. These are overwhelmingly systems with the *TESS* extended mission data, thus having longer time baselines with which to constrain orbital periods. Our fitted periods, however, are generally consistent within uncertainties of their ExoFOP values, and as such we do not report new uncertainties here. Additionally, our least-squares fits to seven of our light curves proved insensitive to non-edge-on inclinations. As such, we report conservative uncertainties of ±5° for these planets.

BT-Settl model atmospheres – much more limited in wavelength coverage than Mann et al. (2015) or our work here.

The interferometric sample shows good agreement, though we observe an ∼70 K temperature systematic of the same sign as for the Mann et al. (2015) sample. However, due to the bias of interferometry towards close and thus bright targets, these are also the brightest stars we observe and they have correspondingly high photometric uncertainties due to saturation. This is particularly acute in the 2MASS bands, where less than half the sample has the photometric quality flag (Qflg) of 'AAA', in contrast to the rest of the standard sample where all but two of 117 stars have Qflg 'AAA', and the entirety of the *TESS* sample. None the less, our derived radii for the interferometric standards (Fig. 8) are consistent when allowing for additional scatter from poor-quality photometry on bright stars that will not be present for our science targets. Encouragingly, however, Mann et al. (2015), which we are in agreement with, integrated their own photometry from low-resolution flux-calibrated spectra and found a good match between their results and their own interferometric sample.

Finally, our results are consistent with our sample of mid-K-dwarfs in the temperature range of our warmest science targets. The observed higher scatter (than e.g. the Mann et al. 2015 sample) is to be expected due to inter-study systematics, as these targets were not pulled from a single uniform catalogue.

While the exact cause of the Mann et al. (2015) and interferometric systematic is unclear, its appearance in both samples suggests it is not an artefact. As such, we apply a −30 K-correction to the observed temperature systematic. Although our remaining scatter is consistent with the scatter in our external reference catalogues, we add a further ±30 K $T_{\rm eff}$ uncertainty in quadrature with our statistical uncertainties to account for the unknown origin of the observed systematic. Given these corrections, we are confident that our fitting methodology is able to recover both accurate and precise stellar temperatures and radii for stars in the range of 3000 K$\lesssim T_{\rm eff} \lesssim$ 4500 K – critical for insight into the radii of their transiting planets.

6.3 Model limitations

The inability of cool dwarf atmospheric models to reproduce optical fluxes is significant. Such wavelengths are among the most easily accessible, and understanding them is required to take full advantage of photometry from surveys like *Gaia* and SkyMapper. Thus, anyone relying directly (e.g. spectral fitting) or indirectly (e.g. isochrone fitting with colours) on models for cool stellar atmospheres must do so with caution (for specifics on isochrone systematics, see e.g. VandenBerg, Bergbusch & Dowler 2006 for the Victoria-Regina models, Dotter et al. 2008 and Joyce & Chaboyer 2018 for DSEP, and Dotter 2016 for MIST).

We identify two key areas for improvement with our models and methods as implemented. The first relates to TiO, the dominant opacity source at optical wavelengths. Comparing high-resolution spectra of M-dwarfs to PHOENIX models and TiO templates, Hoeijmakers et al. (2015) concluded that 'the modelled spectrum of TiO is not representative of the real TiO'. McKemmish et al. (2019) confirmed this discrepancy in the process of validating their updated TiO line list, with their comparisons showing significant improvements in both predicted TiO wavelengths and line depths across the optical when using the updated line list. McKemmish et al.

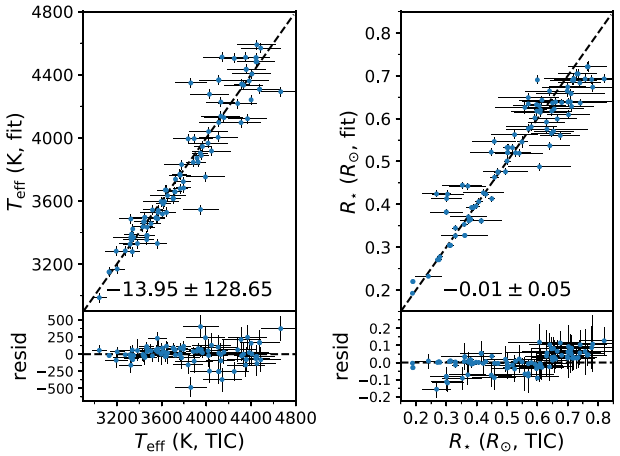

Figure 9. Comparison of $T_{\rm eff}$ and $R_\star$ as reported here compared to those from the *TESS* input catalogue. The median and standard deviation of each set of residuals is annotated.

(2019) were not yet published at the time our MARCS models were generated, and although they note that there remains room for further work, this represents a significant improvement on the previous state-of-the-art. While recomputing our library of synthetic spectra with the new line list would constitute a significant computational effort, we will endeavour to do this in future work.

The second issue concerns proper consideration of the relative abundances of C and O – constituents of the dominant molecular opacity sources in cool dwarf atmospheres – denoted here as [(O–C)/Fe]. As described by Veyette et al. (2016), it is not just $T_{\rm eff}$ and [Fe/H] that affect the location of the pseudo-continuum, but also [(O–C)/Fe]. The principal reason for this is that [(O–C)/Fe] influences the concentrations of C- and O-based molecules, affecting the flux of the pseudo-continuum and apparent strength of metal lines. They conclude that ultimately the inferred value of [Fe/H] depends on [(O–C)/Fe], and that much better spectral fits are possible when allowing [(O–C)/Fe] to vary. An important note is that empirical calibrations based on FGK-M binaries such as Rojas-Ayala et al. (2012), Mann et al. (2013a), and our own photometric [Fe/H] relation should remain valid as statistical [Fe/H] indicators due to the tight Solar Neighbourhood [Fe/H]–[C/O] correlation. Per the recommendation of Veyette et al. (2016), this issue is significant enough to merit new models with [C/Fe] and [O/Fe] as independent parameters.

That said, there is an ever-increasing empirical knowledge of M-dwarfs, meaning that, even in the absence of accurate models, empirical or data-driven approaches should be possible, especially if methods to break the [Fe/H]–[(O–C)/Fe] degeneracy can be found. For instance, see Birky et al. (2020), who demonstrate that a data-driven approach, at least in the *H* band, is possible for M-dwarfs. The very small rate of evolution for these low-mass stars means that we can rely on mass and chemical composition to derive the fundamental parameters of the star, thus making for a more tractable problem.

6.4 *TESS* input catalogue stellar parameters

The *TESS* input catalogue is often the first stellar parameter reference for newly alerted TOIs. As these parameters are mostly derived from empirical relations using literature photometry, we thought it useful to compare these predictions with our fits to inspect for remaining catalogue systematics. Fig. 9 displays this comparison for $T_{\rm eff}$ and $R_\star$, and while the TIC temperatures are broadly consistent, TIC radii for the warmest stars in our sample appear systematically large. This stellar radius systematic is noteworthy as it would bias any predicted exoplanet radii around mid-K dwarfs.

6.5 Emission features in *TESS* candidates

While model limitations prevented us from taking full advantage of our spectra during fitting, our wide wavelength coverage allows us to look for spectral peculiarities. In this study, these take the form of emission in the Hydrogen Balmer Series or Ca II H&K (both signs of stellar activity and youth), as well as absorption in the Li 6708 Å (another sign of youth). While none of our *TESS* planet hosts show detectable Lithium absorption, we report H α equivalent widths and log $R'_{\rm HK}$ in Table 2, calculated using the methodology of Žerjal et al. (2021). 53 stars in our sample have EW H $\alpha > -0.5$ Å (adopted as the limiting bound for activity, noting as well that this is strongly dependent on $T_{\rm eff}$ and thus somewhat approximate), and 35 have log $R'_{\rm HK} > -4.75$ (the lower bound for active stars used in Gray et al. 2006).

Of particular note are our two most active stars, the first of which is TOI 507 (TIC 348538431). TOI 507 appears substantially overluminous in Fig. 1, and presents with strong emission across the Balmer Series and in Ca II H&K. Visual inspection of its spectrum, along with comparison to the cool dwarf standard HIP 103039 that is very similar in $T_{\rm eff}$, indicates that it is actually a double-lined spectroscopic binary. Transit depths appear similar for both primary and secondary eclipses, which points to the system being composed of roughly equal-mass components. Taking an ∼0.75 mag offset into account due to binarity, TOI 507 still sits slightly above the main sequence, meaning that it remains a potentially young touchstone system amenable to characterization as in e.g. Murphy et al. (2020). The mass, radius, $m_{\rm bol}$, and flux reported in Table 2 have been derived for a single component of this binary system, assuming equal mass and brightness.

The second star is TOI 142 (425934411) that is also overluminous and shows strong emission features. Interestingly, it appears to host a giant planet ($R_P = 13.31 \pm 1.39\,{\rm R}_\oplus$) on a short period ($T \approx 0.85$ d) – see Fig. 10. While this is unusual for such a cool star, it is not unheard of, such as K2 32b that is a known short-period super-Neptune orbiting a pre-main-sequence star (David et al. 2016; Mann et al. 2016). Further characterization of the system, however, while scientifically interesting, is likely to be hampered by the faintness of the host star ($G \sim 15.8$).

6.6 Planet parameter recovery

Table E1 (Bayliss et al. (2018), Dreizler et al. (2020), Esposito et al. (2017), Günther et al. (2019), Gilbert et al. (2020), Hartman et al. (2015), Hartman et al. (2020), Huang et al. (2020), Kostov et al. (2019), Luque et al. (2019), Leleu et al. (2021), Mentet al. (2019), Nielsen et al. (2020), Vanderspek et al. (2019), Winters et al. (2019) and Waalkes et al. (2020)) collates literature parameters for previously characterized planets in our sample. These planets have typically had follow-up radial velocity observations, which not only allows for planetary mass determination, but also helps to constrain their orbits when combined with the *TESS* light curves we use here (or additional time series photometric follow-up). Fig. 11 compares these results to our own for $R_P/R_\star$, $a/R_\star$, i, and R_P. We find our results consistent with the literature, aside from a few exceptions discussed below.

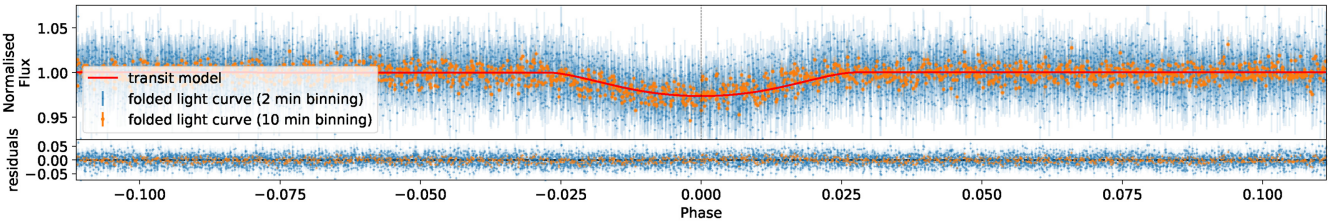

Figure 10. Phase-folded light curve with best-fitting transit model for TOI 142.01.

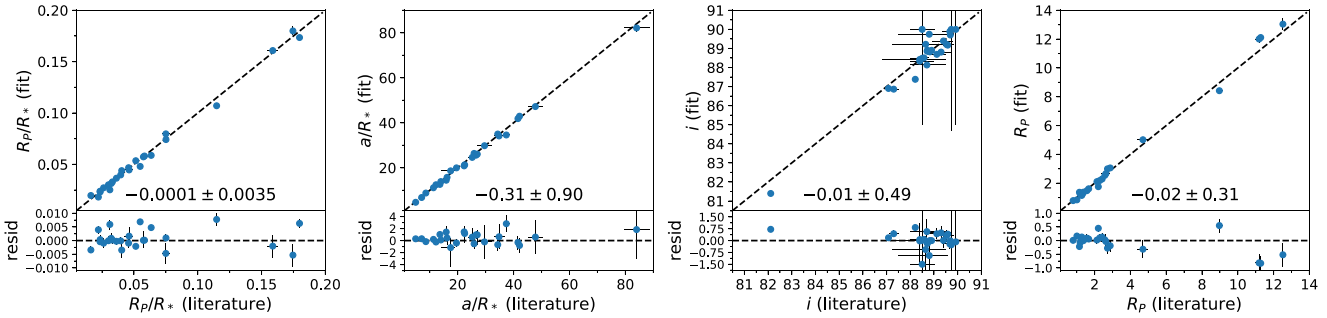

Figure 11. Comparison of $R_P/R_\star$, $a/R_\star$, i, and R_P to literature results in Table E1. Our two largest literature planets, TOIs 129.01 and 551.01, are hot Jupiters in a grazing configuration that leaves their radii poorly constrained. As such, they have been left off for clarity, though our results are consistent within uncertainties. The median and standard deviation of each set of residuals are annotated and exclude these two planets.

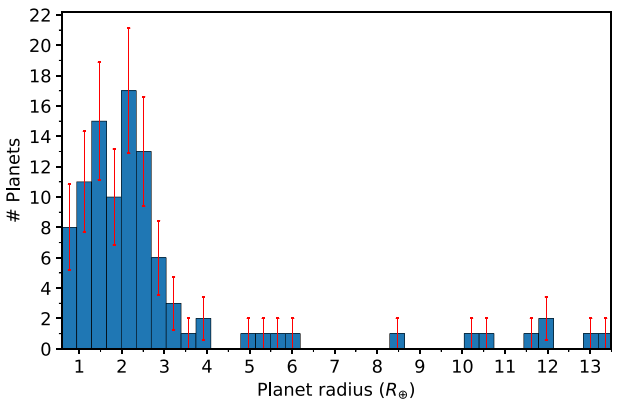

Figure 12. Histogram of candidate planet radii with $R_P < 14\,R_\oplus$, with $0.35\,R_\oplus$ width bins and Poisson uncertainties. Note that we detect the exoplanet radius gap at an $\sim 1\sigma$ level, though remain limited by our small sample size.

6.6.1 LHS 3844 b

Vanderspek et al. (2019) report a larger value of $Rp/R_\star$ for LHS 3844 b (TOI 136.01) than we do here, a difference we can attribute to our access to an extra sector of the *TESS* data. While they also have ground-based data, the extra *TESS* sector amounts to some 60 extra transits, which should give us improved precision.

6.6.2 HATS-48 A b, TOI 178 b/e, and LHS 1140 c

Comparison with HATS-48 A b (TOI 1067.01) from Hartman et al. (2020) shows an inconsistent value of $R_P/R_\star$, indicating a difference in how we have modelled the light curves. While we have access to an additional sector of the *TESS* data, the difference primarily appears to come from (a) including RVs in their fit and (b) their use of an additional 'dilution factor' when fitting to account for nearby unresolved stars. Such nearby stars have the effect of diluting the transit and making the transit appear shallower than it would were only the flux from the host star observed. Our transit fits, by comparison, rely on the quality of the detrending and correction for crowding already done by the *TESS* team and provided in their PDCSAP fluxes.

Leleu et al. (2021) report parameters for six planets orbiting TOI 178, of which only three were alerted on as TOIs. Our parameters are consistent for all but two of these, TOI 178 b (not alerted on) and TOI 178.03, both of which are relatively low-SNR detections by *TESS*. Although our analysis includes an additional *TESS* sector of data, they employ higher precision data from CHEOPS to which we attribute the difference.

The analysis of LHS 1140 c (TOI 256.02) by Ment et al. (2019) results in a value of $R_P/R_\star$ discrepant with our own. While our analysis makes use of an additional sector of the *TESS* data, we consider their results more reliable as they conducted a joint RV and transit photometry analysis, including additional ground-based data alongside the high-precision *Spitzer* data.

6.6.3 WASP-43 b and HATS-6 b

We find a consistent $R_P/R_\star$ with Esposito et al. (2017) for WASP-43 b (TOI 656.01), though our value of R_P is smaller. This difference is attributable to their larger and less precise stellar $T_{\rm eff}$, with which they obtain a smaller stellar radius – resulting in a smaller planetary radius. As discussed, we are confident with our $T_{\rm eff}$ and $R_\star$ recovery, and consider the difference the result of differing approaches to stellar parameter determination.

For HATS-6 b (TOI 468.01), we find our $R_P/R_\star$ and $T_{\rm eff}$ consistent, but a different value for R_P as compared to Hartman et al. (2015). This difference again arises from a smaller literature value of $R_\star$. We

consider our approach to radius determination using stellar fluxes more direct than the modelling-based approach used here, especially given our access to precision *Gaia* parallaxes.

6.7 Candidate planet radius distribution

We plot a histogram of our candidate planet radii in Fig. 12, which shows the existence of the planet radius gap, first identified by Fulton et al. (2017), at $\sim$1.65–2.0 $R_\oplus$ at an $\sim 1\sigma$ level. As we remain limited by our small sample size, we do not perform any additional analysis and leave such investigations for future studies based on a larger sample of *TESS* planets.

Our results, however, do provide encouraging further evidence for the radius gap being present around planets orbiting low-mass stars. Its detection for the stellar mass range considered here is similar to the work of Cloutier & Menou (2020), who investigated a set of confirmed and candidate planets from *Kepler* and *K*2 orbiting stars with $T_{\rm eff} < 4,700$ K, with their sample being roughly a factor of $\sim$4.5 larger than our own. Separating their planets into bins of different stellar mass, they demonstrated that the bimodality in the radius distribution vanishes as stellar mass decreases, corresponding to the population of rocky planets beginning to dominate that of their more gas-rich counterparts. They note, however, that a much larger sample of planets is required in order to properly distinguish between the various possible formation channels for the radius valley (e.g. photoevaporation, core-powered mass-loss), particularly when further subdividing the sample by stellar mass. It is hoped that our results here can contribute to a larger future analysis combining *Kepler*, K2, *and TESS* planets, perhaps also looking into correlations with stellar activity using activity measures such as we provide.

7 CONCLUSIONS

In the work presented above, we have described our ANU 2.3 m/WiFeS observing programme to characterize 92 southern *TESS* candidate planet hosts with $3000\,{\rm K} \lesssim T_{\rm eff} \lesssim 4500\,{\rm K}$ in order to precisely determine the radii of 100 transiting planets they host. In the process of doing so, we investigated cool dwarf model atmosphere systematics, as well as developed a new photometric [Fe/H] calibration. The main conclusions from our work are as follows:

(i) Cool dwarf MARCS model atmospheres systematically overestimate flux in the optical relative to the well-produced spectral regions 5585–6029 Å and 6159–7000 Å, with agreement being worse the cooler the star or bluer the wavelength. We report a simple linear relation parametrizing the offset as a function of the observed *Gaia* $(B_P - R_P)$ colour, enabling the correction of synthetic *Gaia* B_P, and SkyMapper *g* and *r* magnitudes. We recommend future work to consider updated molecular line lists (McKemmish et al. 2019) and non-solar-scaled chemical abundances (see Veyette et al. 2016).

(ii) Using the same models, a general least-squares fitting approach to medium-resolution optical spectra and literature photometry is not sufficient to accurately recover [Fe/H] for cool dwarfs. We instead develop an updated photometric [Fe/H] calibration for cool dwarfs, built using a sample of 69 M and K dwarfs with FGK binary companions having reliable [Fe/H] measurements. By relating the position of these isolated main-sequence KM stars in $M_{K_S} - (B_P - K_S)$ space to the FGK companion, and thus system, [Fe/H], our relation can determine metallicity to a precision of ± 0.19 dex for stars with $1.51 < (B_P - R_P) < 3.3$. This relation expands on the work of Bonfils et al. (2005), Johnson & Apps (2009), and Schlaufman & Laughlin (2010), and takes advantage of precision *Gaia* parallaxes (for precise distances) and kinematics (for binary identification) for the first time.

(iii) We determine $T_{\rm eff}$ and $R_\star$ for our 92 *TESS* candidate planet hosts with a median precision of 0.8 per cent and 1.7 per cent respectively, as well as radial velocities to $\sim 4.5\,{\rm km\,s^{-1}}$. 42 of these targets did not previously have radial velocities from *Gaia* DR2, thus completing the kinematics for these stars.

(iv) We report H α equivalent widths and Ca II H&K $\log R'_{\rm HK}$ for our sample, both signs of activity and youth. None of our stars display detectable Lithium 6708 Å absorption.

(v) We use our derived stellar parameters to fit the *TESS* light curves for our 100 planet candidates in order to determine R_P with a median precision of 3.5 per cent. Our planet properties are consistent with the 30 already confirmed by other studies. We additionally see evidence of the planet radius gap at an $\sim 1\sigma$ level for our low-mass stellar sample, with the robustness of the detection only limited by the small sample size.

(vi) We report the existence of two likely young systems based on stellar emission and location above the main sequence: TOI 507 (TIC 348538431) and TOI 142 (425934411). The former appears to be a near-equal-mass, double-lined eclipsing binary with $T_{\rm eff} \approx 3300$ K, potentially amenable to characterization as a pre-main sequence benchmark system. TOI 142 on the other hand has a giant planet ($R_P = 13.31 \pm 1.39\,R_\oplus$) on a short-period ($T \approx 0.85$ d) orbit.

This is one of the largest uniform analyses of cool *TESS* candidate planet hosts to date, and the first cool dwarf photometric [Fe/H] calibration based on the *Gaia* data. Given the major difficulties encountered using model atmospheres for [Fe/H] determination, we plan to conduct follow-up work investigating empirical or data-driven approaches built upon our now large collection of cool dwarf standard spectra.

ACKNOWLEDGEMENTS

We acknowledge the traditional owners of the land on which the ANU 2.3 m Telescope stands, the Gamilaraay people, and pay our respects to elders past, present and emerging. We also acknowledge helpful early conversations with George Zhou about target selection and observing strategy, as well as the efforts of Andy Casey in developing a prototype data-driven model that ultimately proved out of scope for this study. We thank the anonymous referee for their helpful comments.

ADR acknowledges support from the Australian Government Research Training Program, and the Research School of Astronomy & Astrophysics top-up scholarship. MŽ and MJI acknowledge funding from the Australian Research Council (grant DP170102233). LC is the recipient of the ARC Future Fellowship FT160100402. MJ was supported the Research School of Astronomy and Astrophysics at the Australian National University and funding from Australian Research Council grant no. DP150100250. Parts of this research were conducted by the Australian Research Council Centre of Excellence for All Sky Astrophysics in 3 Dimensions (ASTRO 3D), through project number CE170100013.

This research has made use of the Exoplanet Follow-up Observation Program website, which is operated by the California Institute of Technology, under contract with the National Aeronautics and Space Administration under the Exoplanet Exploration Program. This paper includes data collected by the *TESS* mission. Funding for the *TESS* mission is provided by the NASA Explorer Program. This work has made use of data from the European Space Agency

(ESA) mission *Gaia* (https://www.cosmos.esa.int/gaia), processed by the *Gaia* Data Processing and Analysis Consortium (DPAC; https://www.cosmos.esa.int/web/gaia/dpac/consortium). Funding for the DPAC has been provided by national institutions, in particular the institutions participating in the *Gaia*

Multilateral Agreement. This publication makes use of data products from the Two Micron All Sky Survey, which is a joint project of the University of Massachusetts and the Infrared Processing and Analysis Center/California Institute of Technology, funded by the National Aeronautics and Space Administration and the National Science Foundation. The national facility capability for SkyMapper has been funded through ARC LIEF grant LE130100104 from the Australian Research Council, awarded to the University of Sydney, the Australian National University, Swinburne University of Technology, the University of Queensland, the University of Western Australia, the University of Melbourne, Curtin University of Technology, Monash University, and the Australian Astronomical Observatory. SkyMapper is owned and operated by The Australian National University's Research School of Astronomy and Astrophysics. The survey data were processed and provided by the SkyMapper Team at ANU. The SkyMapper node of the All-Sky Virtual Observatory (ASVO) is hosted at the National Computational Infrastructure (NCI). Development and support of the SkyMapper node of the AS VO has been funded in part by Astronomy Australia Limited (AAL) and the Australian Government through the Commonwealth's Education Investment Fund (EIF) and National Collaborative Research Infrastructure Strategy (NCRIS), particularly the National eResearch Collaboration Tools and Resources (NeCTAR) and the Australian National Data Service Projects (ANDS). This research made use of Lightkurve, a PYTHON package for *Kepler* and *TESS* data analysis.

Software: ASTROPY (Astropy Collaboration 2013), BATMAN (Kreidberg 2015), IPYTHON (Perez & Granger 2007), DUSTMAPS (Green 2018), LIGHTKURVE (Lightkurve Collaboration 2018), MATPLOTLIB (Hunter 2007), NUMPY (Harris et al. 2020), PANDAS (McKinney 2010), and SCIPY (Jones, Oliphant & Peterson 2016).

DATA AVAILABILITY

All fitted stellar and planetary results are available in the article and in its online supplementary material, and stellar spectra will be shared on reasonable request to the corresponding author. All other data used are publicly available.

REFERENCES

Allard F., Hauschildt P. H., Alexander D. R., Starrfield S., 1997, ARA&A, 35, 137
Allard F., Homeier D., Freytag B., 2011, in Christophe M. J.-K., Matthew K. W., Andrew A.W., eds, ASP Conf. Ser. Vol. 448, Cool Stars, Stellar Systems, and the Sun. Astron. Soc. Pac., San Francisco, p. 91
Allard F., Homeier D., Freytag B., 2012a, Phil. Trans. R. Soc. London Ser. A, 370, 2765
Allard F., Homeier D., Freytag B., Sharp C. M., 2012b, in Reylé C., Charbonnel C., Schultheis M., eds, EAS Publ. Ser., Vol. 57, Low-Mass Stars and the Transition Stars/Brown Dwarfs. Roscoff, France, p. 3
Alvarez R., Plez B., 1998, A&A, 330, 1109
Asplund M., Grevesse N., Sauval A. J., Scott P., 2009, ARA&A, 47, 481
Astropy Collaboration, 2013, A&A, 558, A33
Baraffe I., Chabrier G., Allard F., Hauschildt P. H., 1998, A&A, 337, 403
Baraffe I., Homeier D., Allard F., Chabrier G., 2015, A&A, 577, A42
Bayliss D. et al., 2018, MNRAS, 475, 4467
Bean J. L., Sneden C., Hauschildt P. H., Johns-Krull C. M., Benedict G. F., 2006a, ApJ, 652, 1604
Bean J. L., Benedict G. F., Endl M., 2006a, ApJ, 653, L65
Benedict G. F. et al., 2016, AJ, 152, 141
Birky J., Hogg D. W., Mann A. W., Burgasser A., 2020, ApJ, 892, 31
Bonfils X., Delfosse X., Udry S., Santos N. C., Forveille T., Ségransan D., 2005, A&A, 442, 635
Borucki W. J. et al., 2010, Science, 327, 977
Boyajian T. S. et al., 2012, ApJ, 757, 112
Brown A. G. A., et al., 2018, A&A, 616, A1
Caffau E., Ludwig H.-G., Steffen M., Freytag B., Bonifacio P., 2011, Sol. Phys., 268, 255
Carrillo A., Hawkins K., Bowler B. P., Cochran W., Vanderburg A., 2020, MNRAS, 491, 4365
Casagrande L., VandenBerg D. A., 2014, MNRAS, 444, 392
Casagrande L., VandenBerg D. A., 2018a, MNRAS, 475, 5023
Casagrande L., VandenBerg D. A., 2018b, MNRAS, 479, L102
Casagrande L., Schönrich R., Asplund M., Cassisi S., Ramírez I., Meléndez J., Bensby T., Feltzing S., 2011, A&A, 530, A138
Casagrande L., Wolf C., Mackey A. D., Nordlander T., Yong D., Bessell M., 2019, MNRAS, 482, 2770
Casagrande L. et al., 2020, preprint (arXiv:2011.02517)
Cassan A. et al., 2012, Nature, 481, 167
Chabrier G., 2003, PASP, 115, 763
Chabrier G., Baraffe I., 2000, ARA&A, 38, 337
Childress M. J., Vogt F. P. A., Nielsen J., Sharp R. G., 2014, Ap&SS, 349, 617
Claret A., 2017, A&A, 600, A30
Cloutier R., Menou K., 2020, AJ, 159, 211
Crundall T. D., Ireland M. J., Krumholz M. R., Federrath C., Žerjal M., Hansen J. T., 2019, MNRAS, 489, 3625
David T. J. et al., 2016, Nature, 534, 658
da Silva R., Milone A. C., Reddy B. E., 2011, A&A, 526, A71
Delfosse X., Forveille T., Ségransan D., Beuzit J.-L., Udry S., Perrier C., Mayor M., 2000, A&A, 364, 217
Desidera S. et al., 2004, A&A, 420, 683
De Cat P. et al., 2015, ApJS, 220, 19
Dittmann J. A., Irwin J. M., Charbonneau D., Newton E. R., 2016, ApJ, 818, 153
Dopita M., Hart J., McGregor P., Oates P., Bloxham G., Jones D., 2007, Ap&SS, 310, 255
Dotter A., 2016, ApJS, 222, 8
Dotter A., Chaboyer B., Jevremović D., Kostov V., Baron E., Ferguson J. W., 2008, ApJS, 178, 89
Dreizler S. et al., 2020, A&A, 644, A127
Dressing C. D., Charbonneau D., 2015, ApJ, 807, 45
Dressing C. D. et al., 2019, AJ, 158, 87
Esposito M. et al., 2017, A&A, 601, A53
Feiden G. A., Chaboyer B., 2012, ApJ, 757, 42
Fuhrmann K., 2008, MNRAS, 384, 173
Fulton B. J., Petigura E. A., 2018, AJ, 156, 264
Fulton B. J. et al., 2017, AJ, 154, 109
Gaia Collaboration, 2016, A&A, 595, A2
Gaidos E. et al., 2014, MNRAS, 443, 2561
Gilbert E. A. et al., 2020, AJ, 160, 116
Ginzburg S., Schlichting H. E., Sari R., 2018, MNRAS, 476, 759
Gray R. O., Corbally C. J., Garrison R. F., McFadden M. T., Bubar E. J., McGahee C. E., O'Donoghue A. A., Knox E. R., 2006, AJ, 132, 161
Green G. M., 2018, J. Open Source Softw., 3, 695
Günther M. N. et al., 2019, Nat. Astron., 3, 1099
Gupta A., Schlichting H. E., 2019, MNRAS, 487, 24
Gupta A., Schlichting H. E., 2020, MNRAS, 493, 792
Gustafsson B., Edvardsson B., Eriksson K., Jørgensen U. G., Nordlund Å., Plez B., 2008, A&A, 486, 951
Hansen J. T., Casagrande L., Ireland M. J., Lin J., 2021, MNRAS, 501, 5309
Hardegree-Ullman K. K., Zink J. K., Christiansen J. L., Dressing C. D., Ciardi D. R., Schlieder J. E., 2020, ApJS, 247, 28
Harris C. R. et al., 2020, Nature, 585, 357
Hartman J. D. et al., 2015, AJ, 149, 166
Hartman J. D. et al., 2020, AJ, 159, 173

Hawkins K. et al., 2020, MNRAS, 492, 1164
Hejazi N., De Robertis M. M., Dawson P. C., 2015, AJ, 149, 140
Henry T. J., McCarthy D. W., Jr, 1993, AJ, 106, 773
Henry T. J., Kirkpatrick J. D., Simons D. A., 1994, AJ, 108, 1437
Henry T. J., Jao W.-C., Subasavage J. P., Beaulieu T. D., Ianna P. A., Costa E., Méndez R. A., 2006, AJ, 132, 2360
Henry T. J. et al., 2018, AJ, 155, 265
Hinkel N. R. et al., 2016, ApJS, 226, 4
Hoeijmakers H. J., Kok R. J. d., Snellen I. a. G., Brogi M., Birkby J. L., Schwarz H., 2015, A&A, 575, A20
Howard A. W. et al., 2012, ApJS, 201, 15
Howell S. B. et al., 2014, PASP, 126, 398
Huang C. X. et al., 2020, ApJ, 892, L7
Hunter J. D., 2007, Comput. Sci. Eng., 9, 90
Ikoma M., Hori Y., 2012, ApJ, 753, 66
Johnson J. A., Apps K., 2009, ApJ, 699, 933
Jones E., Oliphant T., Peterson P., 2016, SciPy: Open-Source Scientific Tools for Python, 2001
Joyce M., Chaboyer B., 2015, ApJ, 814, 142
Joyce M., Chaboyer B., 2018, ApJ, 856, 10
Keller S. C. et al., 2007, Publ. Astron. Soc. Aust., 24, 1
Kipping D. M., 2008, MNRAS, 389, 1383
Kostov V. B. et al., 2019, AJ, 158, 32
Kraus A. L., Cody A. M., Covey K. R., Rizzuto A. C., Mann A. W., Ireland M. J., 2015, ApJ, 807, 3
Kreidberg L., 2015, PASP, 127, 1161
Kruse E., Agol E., Luger R., Foreman-Mackey D., 2019, ApJS, 244, 11
Kurucz R. L., 1995, Kurucz CD-ROM, 15. Smithsonian Astrophys. Obs., Cambridge
Kuruwita R. L., Ireland M., Rizzuto A., Bento J., Federrath C., 2018, MNRAS, 480, 5099
Kuznetsov M. K., del Burgo C., Pavlenko Y. V., Frith J., 2019, ApJ, 878, 134
Lallement R., Welsh B. Y., Vergely J. L., Crifo F., Sfeir D., 2003, A&A, 411, 447
Lebzelter T. et al., 2012, A&A, 547, A108
Lee E. J., Chiang E., 2016, ApJ, 817, 90
Lee E. J., Chiang E., Ormel C. W., 2014, ApJ, 797, 95
Leggett S. K., Allard F., Berriman G., Dahn C. C., Hauschildt P. H., 1996, ApJS, 104, 117
Leike R. H., Enßlin T. A., 2019, A&A, 631, A32
Leike R. H., Glatzle M., Enßlin T. A., 2020, A&A, 639, A138
Leleu A. et al., 2021, A&A, 649, A26
Lépine S., Hilton E. J., Mann A. W., Wilde M., Rojas-Ayala B., Cruz K. L., Gaidos E., 2013, AJ, 145, 102
Leroy J. L., 1993, A&A, 274, 203
Lightkurve Collaboration, 2018, Astrophysics Source Code Library, recordascl:1812.013
Lindgren S., Heiter U., 2017, A&A, 604, A97
Lindgren S., Heiter U., Seifahrt A., 2016, A&A, 586, A100
Lopez E. D., Fortney J. J., 2014, ApJ, 792, 1
Lopez E. D., Rice K., 2018, MNRAS, 479, 5303
Luck R. E., 2017, AJ, 153, 21
Luck R. E., 2018, AJ, 155, 111
Luck R. E., Heiter U., 2005, AJ, 129, 1063
Luque R. et al., 2019, A&A, 628, A39
Mann A. W., Gaidos E., Lépine S., Hilton E. J., 2012, ApJ, 753, 90
Mann A. W., Brewer J. M., Gaidos E., Lépine S., Hilton E. J., 2013a, AJ, 145, 52
Mann A. W., Brewer J. M., Gaidos E., Lépine S., Hilton E. J., 2013b, Astron. Nachr., 334, 18
Mann A. W., Gaidos E., Ansdell M., 2013c, ApJ, 779, 188
Mann A. W., Feiden G. A., Gaidos E., Boyajian T., von Braun K., 2015, ApJ, 804, 64
Mann A. W. et al., 2016, AJ, 152, 61
Mann A. W. et al., 2019, ApJ, 871, 63
McKemmish L. K., Masseron T., Hoeijmakers H. J., Pérez-Mesa V., Grimm S. L., Yurchenko S. N., Tennyson J., 2019, MNRAS, 488, 2836
McKinney W., 2010, Data Structures for Statistical Computing in Python. p. 51, available at: http://conference.scipy.org/proceedings/scipy2010/mckinney.html
Ment K. et al., 2019, AJ, 157, 32
Mishenina T. V., Soubiran C., Kovtyukh V. V., Korotin S. A., 2004, A&A, 418, 551
Montes D. et al., 2018, MNRAS, 479, 1332
Morton T. D., Swift J., 2014, ApJ, 791, 10
Muirhead P. S., Hamren K., Schlawin E., Rojas-Ayala B., Covey K. R., Lloyd J. P., 2012, ApJ, 750, L37
Muirhead P. S., Dressing C. D., Mann A. W., Rojas-Ayala B., Lépine S., Paegert M., De Lee N., Oelkers R., 2018, AJ, 155, 180
Murphy S. J. et al., 2020, MNRAS, 491, 4902
Neves V. et al., 2012, A&A, 538, A25
Newton E. R., Charbonneau D., Irwin J., Berta-Thompson Z. K., Rojas-Ayala B., Covey K., Lloyd J. P., 2014, AJ, 147, 20
Nielsen L. D. et al., 2020, A&A, 639, A76
Nordlander T. et al., 2019, MNRAS, 488, L109
Önehag A., Heiter U., Gustafsson B., Piskunov N., Plez B., Reiners A., 2012, A&A, 542, A33
Onken C. A. et al., 2019, Publ. Astron. Soc. Aust., 36, e033
Owen J. E., Wu Y., 2013, ApJ, 775, 105
Owen J. E., Wu Y., 2017, ApJ, 847, 29
Pagel B. E. J., Portinari L., 1998, MNRAS, 298, 747
Passegger V. M., Wende-von Berg S., Reiners A., 2016, A&A, 587, A19
Passegger V. M. et al., 2018, A&A, 615, A6
Perez F., Granger B. E., 2007, Comput. Sci. Eng., 9, 21
Plez B., 1998, A&A, 337, 495
Plez B., 2012, Astrophysics Source Code Library, recordascl:1205.004
Prugniel P., Vauglin I., Koleva M., 2011, A&A, 531, A165
Rabus M. et al., 2019, MNRAS, 484, 2674
Rains A. D., Ireland M. J., White T. R., Casagrande L., Karovicova I., 2020, MNRAS, 493, 2377
Rajpurohit A. S., Reylé C., Allard F., Homeier D., Schultheis M., Bessell M. S., Robin A. C., 2013, A&A, 556, A15
Rajpurohit A. S., Reylé C., Allard F., Scholz R.-D., Homeier D., Schultheis M., Bayo A., 2014, A&A, 564, A90
Ramírez I., Allende Prieto C., Lambert D. L., 2007, A&A, 465, 271
Reylé C., Rajpurohit A. S., Schultheis M., Allard F., 2011, in Christophe M. J.-K., Matthew K. W., Andrew A.W., eds, ASP Conf. Ser. Vol. 448, Cool Stars, Stellar Systems, and the Sun. Univ. Washington, Seattle, Washington, p. 929
Ricker G. R. et al., 2015, J. Astron. Telesc. Instrum. Syst., 1, 014003
Robinson S. E., Ammons S. M., Kretke K. A., Strader J., Wertheimer J. G., Fischer D. A., Laughlin G., 2007, ApJS, 169, 430
Rojas-Ayala B., Covey K. R., Muirhead P. S., Lloyd J. P., 2010, ApJ, 720, L113
Rojas-Ayala B., Covey K. R., Muirhead P. S., Lloyd J. P., 2012, ApJ, 748, 93
Ryabchikova T., Piskunov N., Kurucz R. L., Stempels H. C., Heiter U., Pakhomov Y., Barklem P. S., 2015, Phys. Scr., 90, 054005
Savitzky A., Golay M. J. E., 1964, Anal. Chem., 36, 1627
Schlaufman K. C., Laughlin G., 2010, A&A, 519, A105
Skory S., Weck P. F., Stancil P. C., Kirby K., 2003, ApJS, 148, 599
Skrutskie M. F. et al., 2006, AJ, 131, 1163
Sousa S. G., Santos N. C., Israelian G., Mayor M., Monteiro M. J. P. F. G., 2006, A&A, 458, 873
Sousa S. G. et al., 2008, A&A, 487, 373
Sousa S. G., Santos N. C., Israelian G., Mayor M., Udry S., 2011, A&A, 533, A141
Souto D. et al., 2017, ApJ, 835, 239
Souto D. et al., 2018, ApJ, 860, L15
Sozzetti A., Torres G., Latham D. W., Stefanik R. P., Korzennik S. G., Boss A. P., Carney B. W., Laird J. B., 2009, ApJ, 697, 544
Stassun K. G., Torres G., 2018, ApJ, 862, 61
Stassun K. G. et al., 2018, AJ, 156, 102
Stassun K. G. et al., 2019, AJ, 158, 138
Terrien R. C., Mahadevan S., Bender C. F., Deshpande R., Ramsey L. W., Bochanski J. J., 2012, ApJ, 747, L38

Tsantaki M., Sousa S. G., Adibekyan V. Z., Santos N. C., Mortier A., Israelian G., 2013, A&A, 555, A150
Valenti J. A., Fischer D. A., 2005, ApJS, 159, 141
VandenBerg D. A., Bergbusch P. A., Dowler P. D., 2006, ApJS, 162, 375
Vanderspek R. et al., 2019, ApJ, 871, L24
Van Eylen V., Agentoft C., Lundkvist M. S., Kjeldsen H., Owen J. E., Fulton B. J., Petigura E., Snellen I., 2018, MNRAS, 479, 4786
Veyette M. J., Muirhead P. S., Mann A. W., Allard F., 2016, ApJ, 828, 95
Veyette M. J., Muirhead P. S., Mann A. W., Brewer J. M., Allard F., Homeier D., 2017, ApJ, 851, 26
von Braun K. et al., 2012, ApJ, 753, 171
von Braun K. et al., 2014, MNRAS, 438, 2413
Waalkes W. C. et al., 2020, AJ, 161, 13
Winters J. G. et al., 2015, AJ, 149, 5
Winters J. G. et al., 2019, AJ, 158, 152
Wittenmyer R. A. et al., 2020, MNRAS, 496, 851
Woolf V. M., Wallerstein G., 2005, MNRAS, 356, 963
Woolf V. M., Wallerstein G., 2006, PASP, 118, 218
Žerjal M. et al., 2021, MNRAS, 503, 938
Zhao G., Zhao Y.-H., Chu Y.-Q., Jing Y.-P., Deng L.-C., 2012, Res. Astron. Astrophys., 12, 723

SUPPORTING INFORMATION

Supplementary data are available at *MNRAS* online.

Table 2. Final results for *TESS* candidate exoplanet hosts.
Table 3. Final results for *TESS* candidate exoplanets.

Table A1. Observing log for *TESS* candidate exoplanet host stars.
Table B1. Observing log for cool dwarf standards.
Table C1. Final results for cool dwarf standards.
Table D1. Stellar pairs and primary [Fe/H] used for photometric [Fe/H] relation.
Table E1. Non-linear limb darkening coefficients from Claret (2017).
Table F1. Summary of literature properties for already confirmed planets.

Please note: Oxford University Press is not responsible for the content or functionality of any supporting materials supplied by the authors. Any queries (other than missing material) should be directed to the corresponding author for the article.

This paper has been typeset from a TEX/LATEX file prepared by the author.